



Product water mass formation by turbulent density currents from a high-order nonhydrostatic spectral element model

Tamay M. Özgökmen^{a,*}, Paul F. Fischer^b, William E. Johns^a

^a *RSMAS/MPO, University of Miami, Miami, FL, United States*

^b *Mathematics and Computer Science Division, Argonne National Laboratory, Argonne, IL, United States*

Received 13 April 2005; received in revised form 19 May 2005; accepted 19 May 2005

Available online 5 July 2005

Abstract

In light of the pressing need for development of parameterizations of gravity current entrainment in ocean general circulation models, the behavior of turbulent gravity currents in the presence of ambient stratification is studied via numerical simulation, for cases in which equilibrated product water masses are formed. The main objective is to explore how the ambient stratification impacts entrainment and the properties of product water masses, which are of ultimate interest to ocean and climate modelers. Numerical experiments are conducted by employing the high-order nonhydrostatic spectral element model Nek5000. It is investigated how the separation level of the current from the bottom, the propagation speed, the salinity of the product water masses, and the transport and entrainment of the gravity current are affected as a function of the strength of the ambient stratification and the slope angle. Results show that, for the case of constant slope angle and linear ambient stratification, the gravity current separates from the bottom such that the entrained mass flux is independent of the slope angle. The entrainment mass transport, product mass transport, and product salinity then depend only on the ambient stratification, and these quantities are approximated as simple algebraic functions of the ambient stratification parameter that modify the source properties.

© 2005 Elsevier Ltd. All rights reserved.

* Corresponding author.

E-mail address: tozgokmen@rsmas.miami.edu (T.M. Özgökmen).

1. Introduction

Most deep and intermediate water masses of the world ocean are released into the large-scale circulation from high-latitude and marginal seas in the form of overflows. For reasons of mass conservation, this downward transport implies upwelling elsewhere in the ocean, and the resulting overturning circulation affects the large-scale horizontal flow through the stretching term in the vorticity balance (e.g., Gargett, 1984). Model representations of overflows thus determine more than just the properties of intermediate and deep water masses in the ocean. With this background, one can understand why ocean general circulation models (OGCMs) are highly sensitive to detail of the representation of overflows in these models (e.g., Willebrand et al., 2001). Specifically, the entrainment of ambient waters into overflows is recognized as being a prominent oceanic processes with significant impact on the ocean general circulation and on the climate in general (the Gravity Current Entrainment Climate Process Team, <http://www.cpt-gce.org/>).

The seminal investigations by Price et al. (1993), Price and Baringer (1994) reveal that the mixing of overflows with the ambient fluid takes place over very small spatial and time scales. Results from observational programs in the Mediterranean Sea overflow (Baringer and Price, 1997a,b), Denmark Strait overflow (Girton and Sanford, 2003; Girton et al., 2003), Red Sea overflow (Peters et al., 2005; Peters and Johns, 2005), Faroe Bank Channel (Price, 2004), and Antarctic Shelves (Gordon et al., 2004) demonstrate the importance of small-scale mixing processes in the dynamics of overflows and frequently show a high variability of overflow properties in time and space. Detailed, quantitative field observations of the turbulent mixing in overflows are still few (Johnson et al., 1994a,b; Peters and Johns, 2005). Hence, much of our present understanding of mixing in bottom gravity currents is derived from laboratory tank experiments (Ellison and Turner, 1959; Simpson, 1969; Britter and Linden, 1980; Simpson, 1982; Turner, 1986; Simpson, 1987; Hallworth et al., 1996; Monaghan et al., 1999; Baines, 2001; Cenedese et al., 2004; Baines, 2005). Generally, when configured for the small slopes of observed overflows [$<2^\circ$], the dense source fluid cannot accelerate enough within the bounds of typical laboratory tanks [$O(1\text{ m})$] to produce turbulent behavior. For turbulence to occur, laboratory experiments are typically configured with slopes greater than 10° . With the recent advances in numerical techniques and computer power, numerical modeling provides an alternative avenue to investigate these processes. In particular, high-resolution numerical simulations of bottom gravity currents with nonhydrostatic models are now possible (e.g., Özgökmen and Chassignet, 2002; Özgökmen et al., 2003, 2004a,b).

An issue of critical importance for OGCMs and climate-related modeling studies is how overflows equilibrate following fast and localized mixing and what the properties of the equilibrated (or so-called product) water masses are. The great majority of laboratory and numerical experiments have been conducted in the presence of a homogeneous ambient fluid, in which case the bottom density current will plunge down indefinitely while the density difference with respect to the ambient erodes continually, and no equilibrium can be attained. While these studies have been beneficial for developing a basic understanding of mixing in bottom gravity currents, the applicability of the results to real oceanic overflows is ultimately limited by the fact that the ocean interior is not homogeneous, and overflows encounter a stratified ambient fluid while propagating over bottom topography. Therefore, there is a need for detailed and systematic investigations focusing on the properties of equilibrated water masses that form when the density of the bottom gravity

current becomes equal to that of the ambient fluid in a stratified environment and the equilibrated water masses detach from the bottom and propagate into the ocean interior.

In this study, the main objective is to carry out numerical simulations in order to investigate how the ambient stratification impacts the details of mixing in bottom gravity currents and how it influences the depth and properties of product water masses, which are of ultimate interest for ocean and climate modelers. To this end, numerical experiments are conducted by employing a high-order spectral element Navier–Stokes solver Nek5000 (Fischer, 1997; Fischer et al., 2000; Tufo and Fischer, 1999; Fischer and Mullen, 2001). The evolution of a dense water mass released at the top of a sloping wedge at constant angle is explored in the presence of a constant ambient stratification gradient. The investigation examines how the separation level of the current from the bottom, the propagation speed, the salinity of the product water masses, and the transport and entrainment of the gravity current are affected as a function of the strength of the ambient stratification and the slope angle.

Our primary finding is that in the case of constant slope angle and linear ambient stratification, the gravity current separates from the bottom such that the entrained mass flux is approximately independent of the slope angle. The entrainment mass transport, product mass transport, and product salinity then depend only on the ambient stratification, and these quantities are approximated as simple algebraic functions of the ambient stratification parameter that modify the source properties.

The paper is organized as follows. Relevant background information is given in Section 2. In Section 3, the numerical model introduced. The experimental setup and parameters are outlined in Section 4. Results are presented in Section 5, and the principal results and future directions are briefly presented in Section 6.

2. Background

Process studies of overflows have traditionally been conducted by using so-called stream-tube models. These models have been useful in examining the path and bulk properties of the Denmark Strait overflow (e.g., Smith, 1975), Weddell Sea overflow (Killworth, 1977), the Mediterranean overflow (Baringer and Price, 1997b), and initial studies of the Red Sea overflow (Bower et al., 2000). Various simplifications are required in these models, such as steady state, motionless ambient fluid, simple topography, and mixing parameterization (typically based on laboratory experiments). However, OGCMs, in particular those used for computing climate scenarios, have inherent problems in modeling the large-scale effects of overflow plumes. These models cannot reproduce the product of the mixing processes and where they enter into the ocean because of three significant obstacles: (i) issues with vertical coordinate systems, (ii) inadequate model resolution, and (iii) the hydrostatic approximation.

Models dilute the outflow water too strongly (e.g., in geopotential vertical coordinate models), thus destroying outflow signal, or they may not generate enough mixing without explicit parameterizations (e.g., in isopycnal coordinate models), resulting in the “wrong” product waters. It is generally accepted from laboratory experiments (Simpson, 1969) and observations (e.g., Baringer and Price, 1997b) that mixing between density currents and the ambient fluid takes place primarily through vertical shear instability. Overflows have a small vertical scale, typically 100–300 m (Price

and Yang, 1998). The embedded overturns are smaller because of limitations imposed by stable stratification. An explicit representation of mixing in overflows in numerical models requires not only a small vertical grid scale but also a horizontal grid scale small enough to capture the billows forming near the density interface. Oceanic observations indicate that the typical height-to-length ratio of Kelvin–Helmholtz billows is about 0.1 (e.g., Marmorino, 1987). The typical resolution requirements for explicit resolution of billows are 10–30 m in the vertical direction and 100–300 m in the horizontal direction. Since overflows propagate with speeds of $O(1 \text{ ms}^{-1})$, the time scale for the evolution of billows is of $O(100 \text{ s})$. Given the typical spatial resolution of 100 km (5–20 km) and time steps of $O(\text{h})$ in climate (large-scale ocean) models, spatial and time scales to resolve overflows are computationally prohibitive at the present time.

In addition to model resolution and vertical coordinate system, another issue is that most ocean models are based on hydrostatic primitive equations. According to the hydrostatic approximation, the primary dynamical balance in the vertical momentum equation is between the pressure gradient and gravitational buoyancy acceleration terms. Therefore, vertical acceleration terms are omitted, and vertical mixing processes important in the dynamics of overflows are misrepresented.

Because of the importance of overflows, there has been significant effort to address these dynamical and modeling issues. Considerable progress has been achieved in improving the down-slope flow of overflows in geopotential vertical coordinate models (e.g., Beckmann and Döscher, 1997; Winton et al., 1998; Killworth and Edwards, 1999; Nakano and Suginohara, 2002). Also, turbulence closures have been tried in terrain-following models (e.g., Jungclaus and Mellor, 2000), and a mixing parameterization based on laboratory experiments (Turner, 1986) has been implemented in isopycnal models with encouraging results (Hallberg, 2000; Papadakis et al., 2003). Systematic comparisons of different vertical coordinate systems (Ezer and Mellor, 2004; Ezer, 2005) and different OGCMs (Legg et al., 2006) have been conducted.

Monaghan et al. (1999) conducted laboratory experiments of gravity currents in an environment, in which a two-layer ambient stratification with a sharp density interface was used. It was observed that the gravity current splits into one that propagates along the interface of the stratified layers, and another along the bottom of the tank. Baines (2001, 2005) conducted laboratory experiments of bottom gravity currents in the presence of continuous ambient stratification and found that in cases of weak forcing, weak ambient stratification, and high bottom roughness, so-called detrainment takes place, characterized by detachment of wisps of fluid from the gravity current into the ambient.

In parallel and complementary to these efforts with OGCMs and laboratory studies, process modeling is an important avenue in order to improve our understanding and parameterizations of overflow processes. Nonhydrostatic, high-resolution, two-dimensional (2D) simulations of bottom gravity currents conducted by Özgökmen and Chassignet (2002) capture explicitly the major features of these currents seen in laboratory experiments, such as the presence of a head in the leading edge of the dense plume and Kelvin–Helmholtz vortices in the trailing fluid. Subsequently, this model was used to simulate the Red Sea outflow where it flows in a submarine canyon, which naturally restricts motion in the lateral direction such that the use of a 2D model provides a reasonable approximation to the dynamics. Özgökmen et al. (2003) showed that this model adequately captures the general characteristics of mixing in the Red Sea overflow within the limitations of a 2D model. Given the importance of fully three-dimensional (3D) motion induced by rotation, seafloor morphology, and lateral instabilities of coherent structures in the turbulent flow field, a

parallel high-order spectral element Navier–Stokes solver, Nek5000, developed by Fischer (1997), was used to conduct nonhydrostatic 3D simulations of bottom gravity currents by Özgökmen et al. (2004a). The results from this study have been used to calibrate conventional mixing parameterizations (e.g., K-profile parameterization, Large et al., 1994, and Turner’s parameterization, Hallberg, 2000) in a hydrostatic ocean general circulation model (HYbrid Coordinate Ocean Model, HYCOM) for overflow applications (Chang et al., in press). Moreover, recognizing that oceanic overflows follow the seafloor morphology, Özgökmen et al. (2004b) used Nek5000 to study the impact of topographic bumps on entrainment in gravity currents. It was found that a bumpy surface can lead to a significant enhancement of entrainment compared to a smooth surface. The change in entrainment was parameterized as a function of statistical estimates of the amplitude and wave-number parameters of bumps with respect to the background slope.

A logical next step is to use Nek5000 to investigate the impact of ambient stratification on the mixing and the formation of equilibrated water masses.

3. Numerical model

Nek5000 combines the high-order accuracy of spectral methods with the geometric flexibility of traditional finite element methods. The code integrates unsteady incompressible Navier–Stokes equations within Boussinesq approximation. Moreover, Nek5000 handles general three-dimensional flow configurations, supports a broad range of boundary conditions for hydrodynamics, and accommodates multiple-species (passive or active tracer) transport. Here, we give a short description of this code.

The momentum and continuity equations subject to the Boussinesq approximation can be written as follows:

$$\frac{D\mathbf{u}}{Dt} = -\frac{1}{\rho_o} \nabla p + \nu_h \nabla_r^2 \mathbf{u} - g \frac{\rho'}{\rho_o} \hat{\mathbf{z}}, \quad (1)$$

$$\nabla \cdot \mathbf{u} = 0, \quad (2)$$

where $\mathbf{u} = (u, v, w)$ is the velocity vector field; p the pressure; $g = 9.81 \text{ m}^2 \text{ s}^{-1}$, the gravitational acceleration; ν_h the viscosity in the horizontal direction; and $\hat{\mathbf{z}}$ the unit normal vector in vertical direction. The material (total) derivative is

$$\frac{D}{Dt} := \frac{\partial}{\partial t} + \mathbf{u} \cdot \nabla \quad (3)$$

and the anisotropic diffusivity is

$$\nabla_r^2 := \frac{\partial^2}{\partial x^2} + \frac{\partial^2}{\partial y^2} + r \frac{\partial^2}{\partial z^2}, \quad (4)$$

where $r := \nu_v/\nu_h$ is the ratio of vertical to horizontal eddy viscosities. The anisotropic Laplacian is a simple subgrid-scale (SGS) model to represent the peculiar dynamics of stratified flows, in particular the anisotropic mixing. A linear equation of state

$$\rho' = \rho_o(\beta S - \alpha T) \quad (5)$$

is used, where ρ_o is the background water density; $\beta = 7 \times 10^{-4} \text{ psu}^{-1}$ and $\alpha = 2 \times 10^{-4} \text{ }^\circ\text{C}^{-1}$ are the salinity contraction and temperature expansion coefficients, respectively; and S and T are salinity and temperature deviations from a background value, respectively. The equations for salinity and heat transport are

$$\frac{DS}{Dt} = K_h \nabla_r^2 S \quad (6)$$

and

$$\frac{DT}{Dt} = K_h \nabla_r^2 T, \quad (7)$$

where we assume that the vertical and horizontal eddy diffusivities also satisfy $r = K_v/K_h$, and K_h and K_v are the same for temperature and salinity.

The time advancement of (1)–(7) is based on second-order semi-implicit operator-splitting methods developed by Maday et al. (1990) and described by Fischer (1997). The hydrodynamics (1)–(3) are advanced first, with explicit treatment of the buoyancy forcing term, followed by the update of the salinity and temperature transport. Spatial discretization is based on the spectral element method (Patera, 1984; Maday and Patera, 1989; Fischer, 1997), which is a high-order weighted residual technique based on compatible velocity and pressure spaces free of spurious modes. Locally, the spectral element mesh is structured, with the solution, data, and geometry expressed as sums of N th-order Lagrange polynomials on tensor-products of Gauss or Gauss–Lobatto (GL) quadrature points. Globally, the mesh is an unstructured array of K deformed hexahedral elements and can include geometrically nonconforming elements. For problems having smooth solutions, the spectral element method achieves exponential convergence with N , despite having only C^0 continuity (which is advantageous for parallelism). The convection operator exhibits minimal numerical dissipation and dispersion, which is important for high-Reynolds number applications.

Efficient solution of the Navier–Stokes equations in complex domains depends on the availability of fast solvers for sparse linear systems. Nek5000 uses as a preconditioner the additive overlapping Schwarz method introduced by Dryja and Widlund (1987) and developed in the spectral element context by Fischer (1997) and Fischer et al. (2000). The key components of the overlapping Schwarz implementation are fast local solvers that exploit the tensor-product form and a parallel coarse-grid solver that scales to thousands of processors (Tufo and Fischer, 2001). The capabilities of the spectral element method have been significantly enhanced through the recent development of a high-order filter that stabilizes the method for convection dominated flows without compromising spectral accuracy (Fischer and Mullen, 2001). More details on the solution procedure of Nek5000 in the context of gravity current simulations can be found in Özgökmen et al. (2004a).

4. Model configuration and parameters

The main experimental strategy is as follows. The behavior of the density current and the product water mass formation are investigated by varying the ambient stratification, which is

initialized by using a linear temperature profile. Given the sensitivity of entrainment to the slope angle (Ellison and Turner, 1959; Turner, 1986; Price and Baringer, 1994; Özgökmen and Chassignet, 2002; Özgökmen et al., 2003), the slope angle is also varied. Therefore, the main experimental parameter matrix consists of six different ambient temperature gradient values and three different slope angles (18 experiments). Because of the large number of experiments considering the computational burden of 3D calculations (about 100-fold higher than for 2D), the great majority of the experiments are conducted in 2D mode. A selected 3D experiment is conducted to quantify the differences from 2D results.

The domain geometry, boundary conditions, and initialization are based on that used in Özgökmen et al. (2004a,b). The model domain is configured with a horizontal length of $L_x = 20$ km. The depth of the water column ranges from $h_i = 400$ m at $x = 0$ to $H = 1000$ m over a constant slope (Fig. 1a). Three slope angles of $\theta = 3^\circ, 5^\circ, 7^\circ$ are used, which are within the general range of oceanic overflows prior to their separation from the bottom, such as the Red Sea overflow entering the Tadjura Rift (e.g., Özgökmen et al., 2003). Geometries with smaller slope angles require a longer domain, and are computationally more expensive.

The boundary conditions at the bottom are no-slip and no-normal flow for the velocity components and no-normal flux, $\partial S/\partial \mathbf{n} = \partial T/\partial \mathbf{n} = 0$ with \mathbf{n} being the normal direction to the boundary, for salinity and temperature. At the top boundary, free-slip and rigid-lid boundary conditions are used. The model is entirely driven by the velocity and salinity forcing profiles at the inlet boundary at $x = 0$ (Fig. 1a and b). A salinity anomaly with an amplitude of $\Delta S = 1$ psu and initial thickness of $h_o = 200$ m is placed at the top of the slope. The velocity distribution at the inlet matches no-slip at the bottom and free-slip at the top using fourth-order polynomials such that the depth integrated mass flux across this boundary is zero. The amplitude of the inflow velocity profile is made time dependent and scaled with the propagation speed of the gravity current, which is zero at $t = 0$ and reaches a constant value shortly after the release. The interior is initialized by using a linear temperature distribution (Fig. 1c). Outflow boundary conditions of the type $\partial \mathbf{u}/\partial x = \partial S/\partial x = \partial T/\partial x = 0$ are used at the exit boundary at $x = L_x$. The propagation of the density front generates internal waves in the ambient stratification, part of which reflect back from the exit boundary. The integrations are terminated before the reflected internal waves interact with the gravity current.

In the 3D case, the domain is extended by $L_y = 2$ km in the spanwise direction, periodic boundary conditions are applied at the lateral boundary, and a sinusoidal perturbation in the initial salinity distribution in the y -direction is employed to facilitate transition to 3D turbulent flow (Fig. 1d).

Model parameters can also be discussed in terms of nondimensional parameters $Ra = (g\beta\Delta S h_o^3)/\nu_h^2$ the Rayleigh number, the ratio of the strengths of buoyancy and viscous forces, $Pr = \nu_h/K_h$ the Prandtl number, the ratio of viscosity and diffusivity, $r = \nu_v/\nu_h = K_v/K_h$ the diffusivity ratio, and $R_\rho = (\alpha\Delta T h_o)/(\beta\Delta S H)$ the density ratio, the ratio of the density gradients due to ambient temperature stratification and overflow salinity stratification. Since Ra represents the range of turbulent scales, the highest Ra permitted by the numerical resolution is used, and $Ra = 8 \times 10^5$ in the experiments presented below. The impact of turbulent motion is assumed to be much higher than that of molecular diffusivities on the effective subgrid-scale diffusion, such that there is no difference between turbulent viscosity and diffusivity, and $Pr = 1$. This assumption is based on the studies by Webster (1964), Rohr et al. (1988) and Schumann and Gerz (1995), which show that the turbulent Pr in the case of strongly mixing shear flows is around unity.

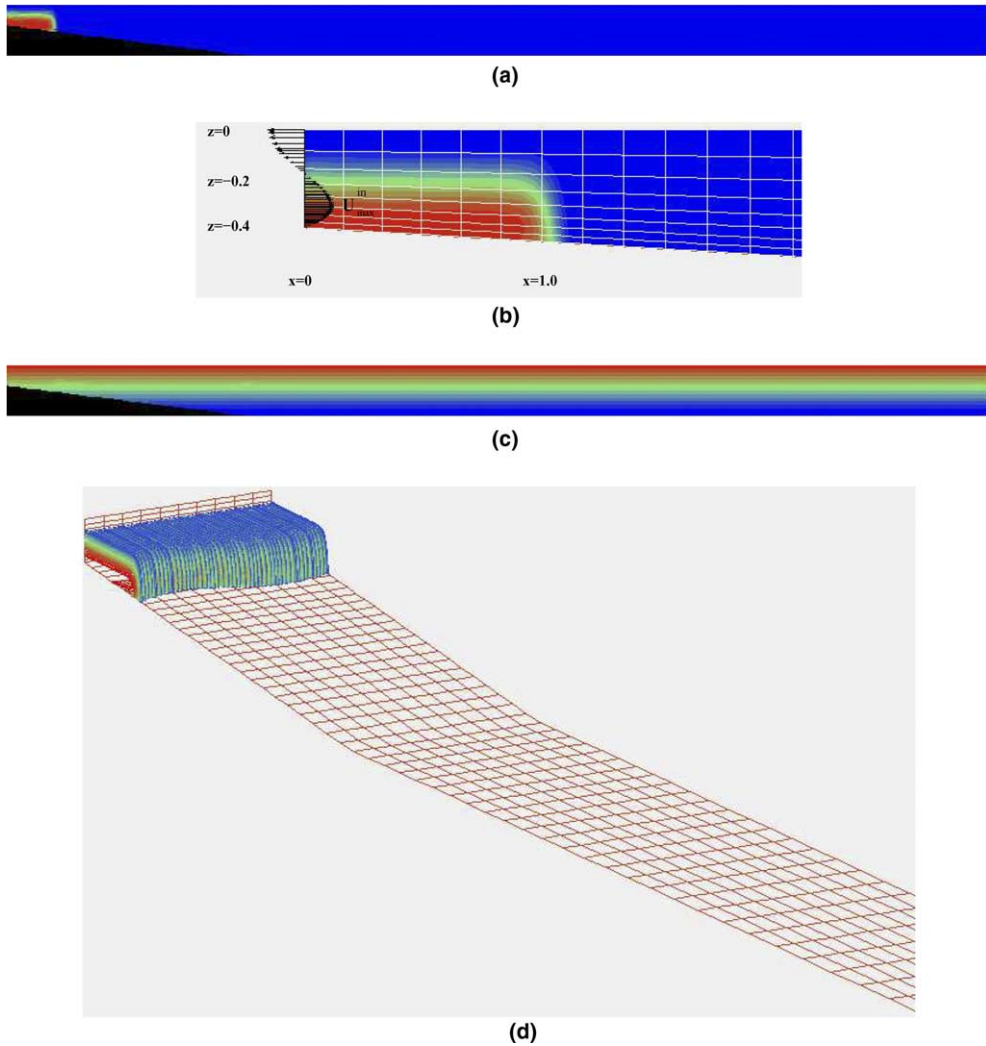


Fig. 1. (a) Domain geometry in 2D for the case with $\theta = 7^\circ$ and initial distribution of salinity; (b) velocity profile at the forcing boundary; (c) initial temperature distribution and (d) domain geometry and salinity initialization in 3D for the case with $\theta = 7^\circ$ (part of the domain is shown). Distribution of elements is depicted in the background.

The anisotropic Laplacian (4) is a simple SGS model used in our simulations, which can be considered in the category of large eddy simulations (LES). LES refers to 3D nonhydrostatic simulations in which the largest eddies are simulated, through computation, and the effect of the smaller eddies on the flow is represented by using SGS models. The main underlying concept is the striking feature of a turbulent flow field in that, while large eddies migrate across the flow, they carry smaller-scale disturbances with them. Large eddies carry most of the Reynolds stress and must be computed, while smaller eddies contribute much less to Reynolds stresses. The LES approach lies in between the extremes of direct numerical simulation, in which all turbulence is resolved, and Reynolds-averaged Navier–Stokes, in which all turbulence is modeled. A diffusivity

ratio of $r = 2 \times 10^{-2}$ is used as in Özgökmen et al. (2004a). Our results do not show a significant difference when other SGS models based on the full deformation tensor (e.g., Smagorinsky, 1963) are employed.

Six values of density ratios are used, $R_\rho = 0; 0.25; 0.34; 0.4; 0.5; 0.6$, which correspond to temperature differences between the top and bottom of the domain of $\Delta T = 0^\circ\text{C}; 4.375^\circ\text{C}; 5.95^\circ\text{C}; 7.0^\circ\text{C}; 8.75^\circ\text{C}; 10.5^\circ\text{C}$, respectively. The corresponding buoyancy periods $T_a = 2\pi/N$, where $N^2 = -\frac{g}{\rho_o} \frac{d\rho'_a}{dz} = g \frac{\alpha\Delta T}{H}$, are $T_a \approx \infty; 2144\text{ s}; 1838\text{ s}; 1693\text{ s}; 1515\text{ s}$ and 1384 s . One can contrast these values to those that the Mediterranean overflow encounters during its descent ($2550\text{ s} \geq T_b \geq 1540\text{ s}$) and that the Red Sea overflow encounters where it descends into the Tadjura Rift ($2820\text{ s} \geq T_b \geq 1140\text{ s}$). Hence, the parameter range in these experiments is applicable to such oceanic situations. The model is integrated for 30,000 s, which is approximately 14- to 22-fold longer than the buoyancy periods.

The reason for the selection of these density ratios is as follows. The maximum separation depth of the overflow can be estimated by calculating where the densest overflow water mass would equilibrate in the ambient fluid in the absence of mixing, namely,

$$-\frac{g}{\rho_o} \frac{d\rho'_a}{dz} = \frac{g}{\rho'_o} \frac{\rho'_o - \rho'_a(z = -h_i)}{D}, \quad (8)$$

where subscripts ‘a’ and ‘o’ stand for ambient and overflow respectively, $h_i = 400\text{ m}$ is the inlet depth, and D is the depth of separation below the inlet. Substituting $\rho'_o = \beta\Delta S - \alpha T(z = -h_i)$, $\rho'_a(z = -h_i) = -\alpha T(z = -h_i)$, $d\rho'_a/dz = \rho_o\alpha\Delta T/H$, we obtain $D = h_o/R_\rho$, or separation depth of

$$h_s = h_i + \frac{h_o}{R_\rho}. \quad (9)$$

For selected stratifications of $R_\rho = 0.34, 0.4, 0.5$ and 0.6 , the lift from the bottom takes place at depths of $h_s = 988\text{ m}, 900\text{ m}, 800\text{ m}$ and 733 m , respectively. Homogeneous experiments with $R_\rho = 0$ are conducted for reference. Experiments with $R_\rho = 0.25$ or $h_s = 1200\text{ m}$ do not separate from the bottom within the total domain depth of $H = 1000\text{ m}$, but they are used to explore the impact of weak stratification on entrainment.

Baines (2001, 2005) conducted laboratory experiments of bottom gravity currents in the presence of ambient stratification, and found that in some cases the so-called detrainment takes place, which is characterized by detachment of wisps of fluid from the gravity current into the ambient. Baines (2005) quantified the regime in which detrainment occurs as a function of the so-called buoyancy number

$$B = \frac{Q_0 N^3}{g_0^2}, \quad (10)$$

where Q_0 is the volume flux (per unit width) of the gravity current, g_0' its initial reduced gravity, and N the ambient stratification frequency. For lock exchange flows, such as the present experiments, $Q_0 \approx \sqrt{g_0' h_o} h_o$ (Benjamin, 1968, also Fig. 7 of Özgökmen et al., 2004a), and since $N^2 = g \frac{\alpha\Delta T}{H}$, we find that

$$B \approx R_\rho^{3/2} \quad (11)$$

Baines (2005) found that detrainment takes place as a complex function of B , entrainment parameter, bottom drag coefficient, and slope angle, but the maximum values of B above which detrainment was not observed are $B = 0.045$ for $\theta = 12^\circ$, $B = 0.009$ for $\theta = 20^\circ$, and $B = 0.005$ for $\theta = 30^\circ$ over a smooth bottom surface. The stratified experiments conducted in this study are the regime of $0.125 \leq B \leq 0.46$ for $3^\circ \leq \theta \leq 7^\circ$, and therefore, we do not anticipate encountering detrainment.

An important factor in the dynamics of oceanic overflows is rotation. The scale at which the Coriolis force becomes comparable to buoyancy force is a complex function of the slope angle, stratification, and friction (e.g., Griffiths, 1986). A simple spatial scale for rotational effects to become important is given by the radius of deformation $\sqrt{g'h}/f_o$, which with the experimental parameters is approximately 52 km; 16 km and 9 km at selected low (10°N), middle (30°N), and high (60°N) latitudes, respectively, as compared to $L_x = 20$ km. The rotation time scale is $2\pi f_o^{-1} \approx 29 \times 10^4$ s; 10×10^4 s, and 6×10^4 s for these latitudes, while the integrations last for 3×10^4 s. Far away from the separation point, one would expect lenses (“Meddies”, Bower et al., 2002) to form because of the effect of rotation. Hence, the results presented here apply to the phase before the impact of rotation starts influencing the flow patterns, and will be relevant for middle- and low-latitude overflows, such as the Mediterranean and Red Sea overflows. In this sense this study complements other process studies focusing on the larger-scale behavior (e.g., Papadakis et al., 2003; Ezer and Mellor, 2004; Ezer, 2005; Legg et al., 2006).

The spectral element method offers a dual approach to convergence: algebraic via elemental grid refinement, and exponential via increase in the order of intra-element interpolation. We therefore chose to use a minimum number of elements so that the shape of the domain geometry is adequately captured and the element size is adjusted to better capture the bottom boundary layer. Once the element distribution satisfies these criteria, we increase the spectral truncation degree for the convergence of the technique. In general, the numerical solution of the physical

Table 1
Parameters of the numerical simulations

Domain size ($L_x, L_z = H, L_y$)	In 2D: (20×10^3 m, 10_3 m); in 3D: (20×10^3 m, 10^3 m, 2×10^3 m)
Slope angles	$\theta = 3^\circ, 5^\circ, 7^\circ$
Rayleigh number	$Ra = 8 \times 10^5$
Prandtl number	$Pr = 1$
Diffusivity ratio	$r = 2 \times 10^{-2}$
Density ratios	$R_\rho = 0, 0.25, 0.34, 0.40, 0.50, 0.60$
Viscosities	$\nu_h = 0.83 \text{ m}^2 \text{ s}^{-1}$ and $\nu_v = 1.66 \times 10^{-2} \text{ m}^2 \text{ s}^{-1}$
Diffusivities	$K_h = 0.83 \text{ m}^2 \text{ s}^{-1}$ and $K_v = 1.66 \times 10^{-2} \text{ m}^2 \text{ s}^{-1}$
Overflow salinity range	$\Delta S = 1.0$ psu
Overflow input thickness	$h_o = 200$ m
Ambient temperature range	$\Delta T = 0, 4.375, 5.95, 7.000, 8.75, 10.5$ °C
Ambient buoyancy period	$T_b = \infty, 2144(36), 1838(31), 1693(28), 1515(25), 1384(23)$ s (min)
Number of elements (x, z, y)	in 2D: (60, 10); and in 3D: (60, 10, 10)
Polynomial degree	$N = 6$
Number of grid points	in 2D: 21,600 and in 3D: 1,296,000
Time step	$\Delta t = 1.2$ s
Total integration time	30,000 s

problem of interest benefits from two well-known features of spectral element models: the lack of numerical dissipation and excellent phase properties.

The 2D mesh has $K = 600$ elements (60×10 in x, z directions), and the 3D mesh has $K = 6000$ elements ($60 \times 10 \times 10$ in x, z, y directions). The elements have a smaller vertical scale toward the bottom boundary and follow topography (Fig. 1d). The results presented in this paper are obtained by using spectral truncation with a polynomial degree of $N = 6$, which corresponds to 21,600 gridpoints for the 2D case and 1,296,000 gridpoints in the 3D case. With a time step of $\Delta t = 1.2$ s, the Courant number remains $C < 1$ throughout the simulations. The model parameters are summarized in Table 1.

5. Results

5.1. Description

Fig. 2 shows the evolution of the salinity distribution in a selected 2D experiment ($\theta = 7^\circ$ and $R_\rho = 0.5$). The system is initialized as described in Section 4 and starts from rest. The initial development of the system is that of the so-called lock-exchange flow (e.g., Keulegan, 1958; Simpson, 1987), in which the lighter fluid remains on top and the denser overflow propagates downslope. The dense gravity current quickly develops a characteristic head at the leading edge (Fig. 2a). The head is half of a dipolar vortex, which is a generic flow pattern that tends to form in two-dimensional systems by self-organization of the flow (e.g., Flierl et al., 1981; Nielsen and Rasmussen, 1996) and which corresponds to the most probable equilibrium state maximizing entropy (Smith, 1991). The head grows and is diluted as the gravity current travels further down the slope, the result of entrainment of fresh ambient fluid. The instability near the top of the trailing fluid

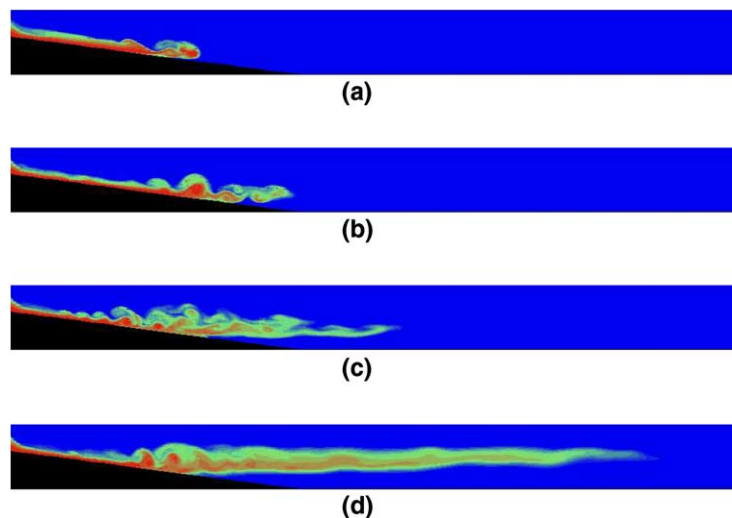


Fig. 2. Salinity distribution in the 2D experiment with $\theta = 7^\circ$ and $R_\rho = 0.5$ at different times: (a) $t = 3000$ s; (b) $t = 5640$ s; (c) $t = 10,200$ s and (d) $t = 26,400$ s.

leads to a rolling up of the density interface in lumped vortices, which is clearly indicative of the Kelvin–Helmholtz instability, in which waves made up of fluid from the current entrap the ambient fluid (e.g., Corcos and Sherman, 1984). Before the gravity current reaches the lower boundary of the domain, the nose of the current lifts off the bottom and starts propagating into the interior ambient fluid (Fig. 2b–d). Mixing persists over the slope but dies off away from the separation point. This process leads to the formation of a high-salinity water mass, which is equilibrated at mid-depth. The corresponding evolution of the temperature distribution is depicted in Fig. 3.

The evolution of the salinity in the equivalent 3D experiment is shown in Fig. 4. As the gravity current starts from rest, the initial spanwise perturbation (Fig. 1d) actually decays such that the current becomes nearly 2D at the beginning (Fig. 4a). But as the system gains enough inertia, perturbations amplify leading to distinct 3D patterns. The gravity current shows signs of equilibration at multiple levels shortly after the separation from the bottom (Fig. 4b,c), which could be due to higher dilution and mixing of the interface between the gravity current and the ambient fluid with respect to the layer near the very bottom. This pattern does not last long, however, as the product water mass achieves coherence away from the slope. Following this initial transient, the salinity surface becomes free from turbulent overturns far away from the slope, thus indicating that no significant turbulent mixing takes place to change further the properties of the product water mass, and most turbulent mixing is confined to that occurring over the slope. Quantitative differences between 2D (Fig. 2) and 3D (Fig. 4) cases are not apparent visually and are investigated below.

By selecting experiments for all slope angles, $\theta = 3^\circ, 5^\circ, 7^\circ$, and with the weakest and strongest ambient stratification leading to separation from the bottom, $R_\rho = 0.34$ and $R_\rho = 0.60$, respectively, snapshots of the salinity fields in Fig. 5 illustrate qualitatively the impact of θ and R_ρ on the behavior of the density current: For small (large) θ , the density current travels a longer (shorter) horizontal distance before reaching the separation point, and mixing is less (more) intense. In

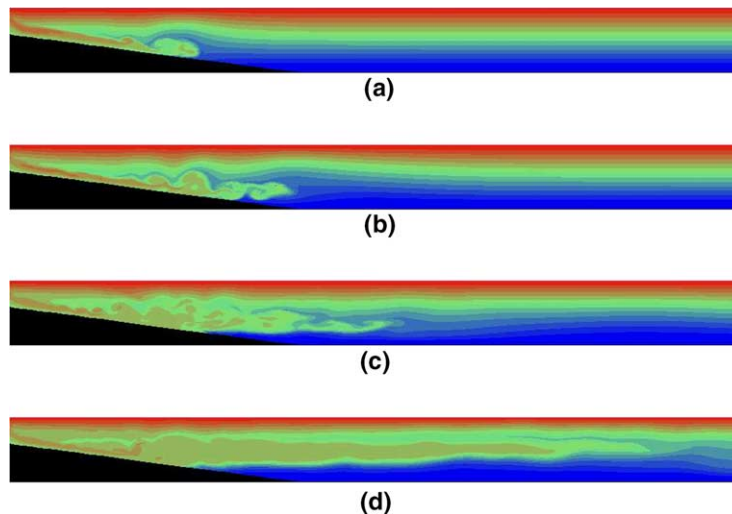


Fig. 3. Temperature distribution in the 2D experiment with $\theta = 7^\circ$ and $R_\rho = 0.5$ at different times: (a) $t = 3000$ s; (b) $t = 5640$ s; (c) $t = 10,200$ s and (d) $t = 26,400$ s.

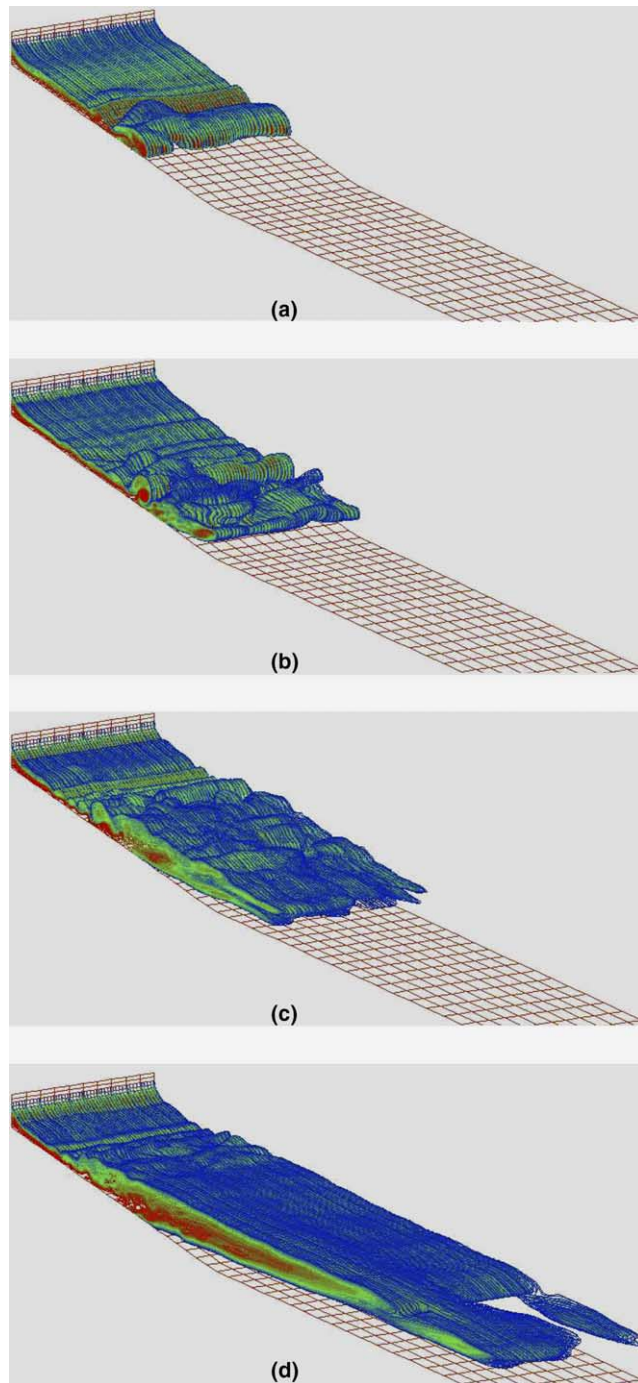


Fig. 4. Salinity distribution in the 3D experiment with $\theta = 7^\circ$ and $R_\rho = 0.5$ at different times: (a) $t = 3000$ s; (b) $t = 5640$ s; (c) $t = 10,200$ s and (d) $t = 26,400$ s. Animation is available from <http://www.rsmas.miami.edu/personal/tamay/3D/ts21-S.gif>.

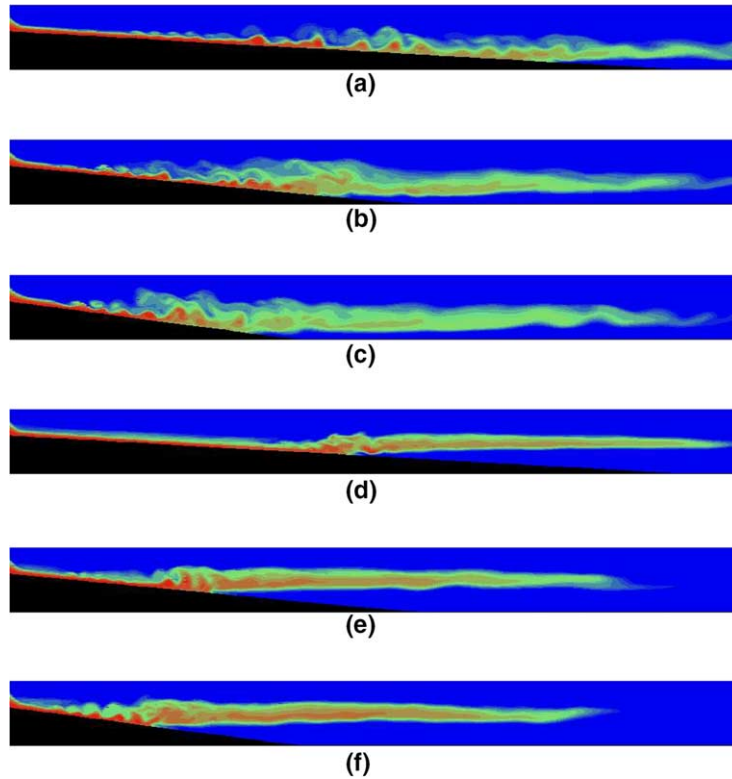


Fig. 5. Snapshots of the salinity distribution at $t = 26,400$ s, in selected experiments: (a) $\theta = 3^\circ$, $R_\rho = 0.34$; (b) $\theta = 5^\circ$, $R_\rho = 0.34$; (c) $\theta = 7^\circ$, $R_\rho = 0.34$; (d) $\theta = 3^\circ$, $R_\rho = 0.60$; (e) $\theta = 5^\circ$, $R_\rho = 0.60$ and (f) $\theta = 7^\circ$, $R_\rho = 0.60$.

all cases, there is significant thickening of the product water masses with respect to the bottom gravity current. This implies reduced propagation speed of the current following its separation with respect to that over the bottom topography and explains why the nose the salinity tongue with $\theta = 3^\circ$ leads those for higher slope angles. As R_ρ gets larger, the separation point moves upward in the water column, as is expected from (9). As R_ρ increases, mixing appears to be gradually suppressed, leading to more saline product water masses. This is because the strengthening of the ambient stratification reduces vertical displacements, and therefore the turbulent overturning scales. Also, the entire thickness of the separated salinity tongue decreases with increasing R_ρ .

However, there seems to be no significant change in the salinity of the product water masses as a function of θ (Fig. 5a vs. 5b vs. 5c, or Fig. 5d vs. 5e vs. 5f). Given the well-known sensitivity of entrainment on the slope angle (Turner, 1986; Price and Baringer, 1994; Baines, 2001; Özgökmen and Chassignet, 2002; Özgökmen et al., 2003), this result seems counter intuitive and is investigated in the following.

5.2. Separation level

The level of equilibration of the gravity current is of interest. Eq. (9) indicates that gravity currents will separate from the bottom within this particular domain ($h_s \leq H$) provided that

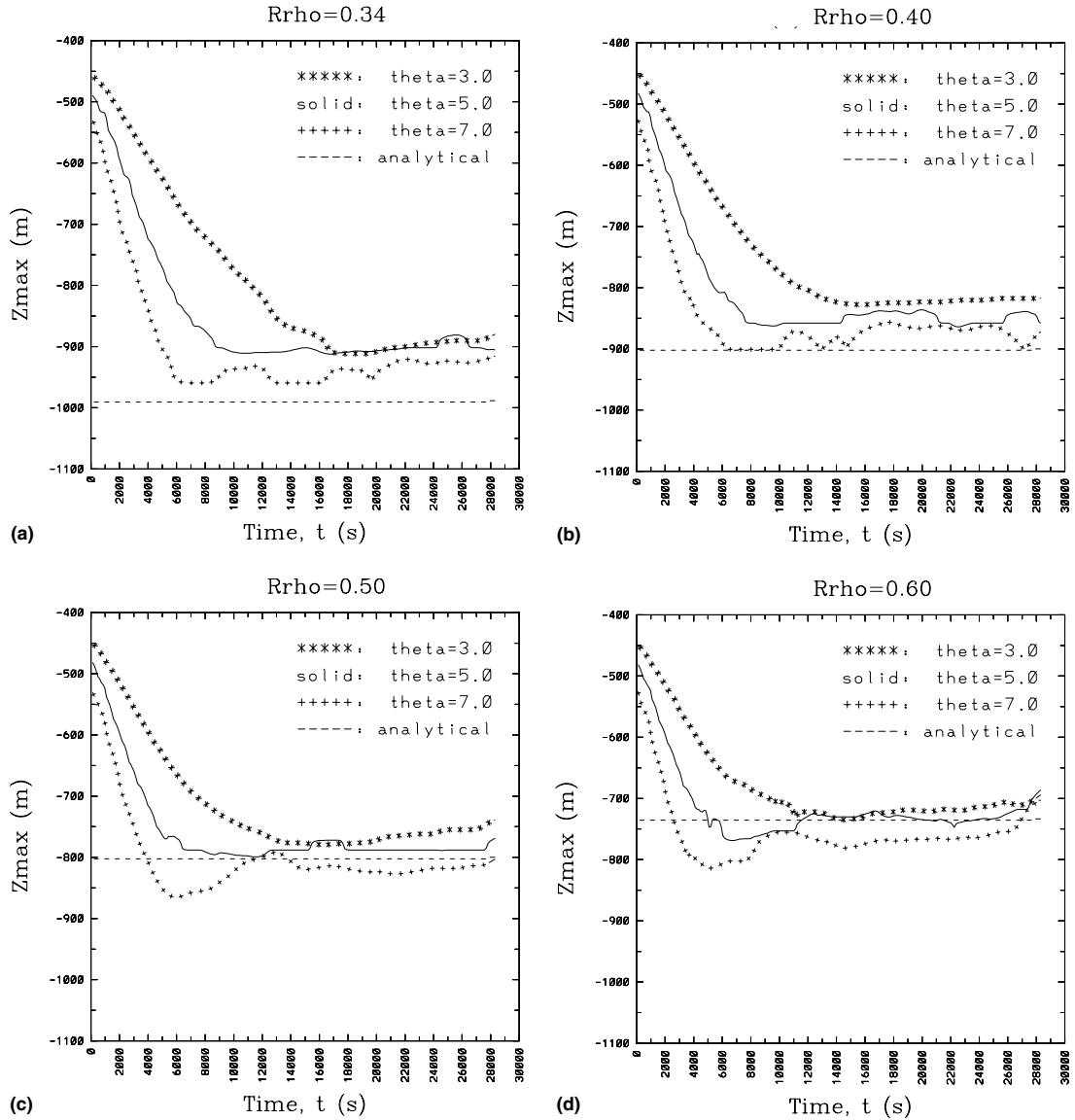


Fig. 6. Maximum depths of the salinity signal associated with the gravity current over the slope as a function of time, $z_{\max}(t)$, for experiments exhibiting separation from the bottom. Those for: (a) $R_{\rho} = 0.34$; (b) $R_{\rho} = 0.40$; (c) $R_{\rho} = 0.50$ and (d) $R_{\rho} = 0.60$. Lines with “***” denote results for $\theta = 3^\circ$, solid lines denote results for $\theta = 5^\circ$, lines with “+++” denote results for $\theta = 7^\circ$ and dashed lines denote $z_{\max} = -h_s$ estimated from (9).

$R_{\rho} \geq 1/3$. Fig. 6 shows the minimum vertical level of the salinity signal associated with the gravity currents as a function of time for all separating experiments, namely, those with $R_{\rho} = 0.34$, $R_{\rho} = 0.40$, $R_{\rho} = 0.50$, and $R_{\rho} = 0.60$, over all three slope angles. Following the initial transient, an equilibrium level is attained in all these experiments. The time the gravity currents take to reach the equilibrium is longer when θ is smaller because a larger distance needs to be travelled before

separation (Fig. 5). The equilibrium separation level changes primarily as a function of R_ρ , while it also shows some sensitivity to θ within the parameter range. For small R_ρ , when vertical displacements and turbulent overturning are less inhibited and mixing is high, the separation equilibrium level is less than that is estimated from (9); for example, separation takes place “prematurely” by ≈ 100 m and ≈ 50 m higher up in the water column for $R_\rho = 0.34$ (Fig. 5a) and $R_\rho = 0.40$, respectively. This indicates that in these cases the mixing layer penetrates all the way through the gravity current and dilutes the densest part near the very bottom (e.g., Fig. 5a–c). As R_ρ increases, the influence of the mixing with the ambient fluid is limited to the upper part of the gravity current, and the densest bottom salinity remains nearly undiluted (Fig. 5e–f). Therefore, Eq. (9) accurately estimates the separation equilibrium level (Fig. 5c and d for $R_\rho = 0.40$ and $R_\rho = 0.50$, respectively). In these cases, however, the gravity current can initially exceed the separation level, which is similar to the so-called overshoot and springback phenomenon observed for turbulent fountains (Bloomfield and Kerr, 1998) and plumes (Baines, 2002) in stratified environments.

5.3. Propagation speed

It is well known that in lock-exchange flows (e.g., Keulegan, 1958) and for constant-flux gravity currents (e.g., Ellison and Turner, 1959; Britter and Linden, 1980), the density front quickly reaches a constant speed of propagation. The propagation speed is insensitive to variations in slope angle because the increase in gravitational force from the greater slope angle is compensated by buoyancy gain from increased entrainment. But these results have been obtained on the basis of experiments conducted in a homogeneous ambient fluid.

The propagation speed, $U_F(t) = dX_F/dt$, where X_F is the position of the nose of the gravity current, is shown in Fig. 7a for all experiments for the case with $\theta = 5^\circ$ (similar results, obtained for $\theta = 3^\circ$ and $\theta = 7^\circ$, are not shown). In the case of a homogeneous environment, $R_\rho = 0$, the current reaches a nearly constant speed of $U_F = 0.85 \text{ ms}^{-1}$ (this experiment was terminated once the gravity current reached the end of the slope). In all other cases in a stratified environment, the propagation speed is initially the same as that for $R_\rho = 0$ but then decreases gradually until a minimum is reached. This dip in U_F is achieved earlier in time when R_ρ increases, since it is associated with the separation from the bottom. Then U_F bounces back to a somewhat higher level and converges to similar values in all experiments for propagation into the interior ocean.

A somewhat different perspective can be gained when U_F is plotted as a function of $z_{\max}(t)$, the maximum depth attained by the gravity currents during their evolution. Fig. 7b illustrates that, while U_F is approximately constant for $R_\rho = 0$, it decreases as R_ρ increases. When the separation depth is achieved, the currents experience a significant reduction in their propagation speed, but the propagation resumes, albeit at the same depth $z_{\max}(t)$. The overshoot and springback phenomenon can also be seen clearly for $R_\rho = 0.50$ and $R_\rho = 0.60$ in Fig. 7b.

The results shown in Fig. 7b can be partially explained by considering that in a two layer system, $U_F = \sqrt{g'h_o(h_i - h_o)/h_i}$, and since $h_i = 2h_o$, $U_F = \frac{1}{\sqrt{2}}\sqrt{g'h_o}$ (see also Fig. 7 of Özgökmen et al., 2004a). Since $g' = g(\rho'_o - \rho'_a)$, we substitute $\rho'_o = \beta\Delta S - \alpha\Delta T(1 - h_i/H)$ and $\rho'_a = -\alpha\Delta T(1 - z'/H)$, where z' is the depth of the water column starting from the top of the domain, and we obtain

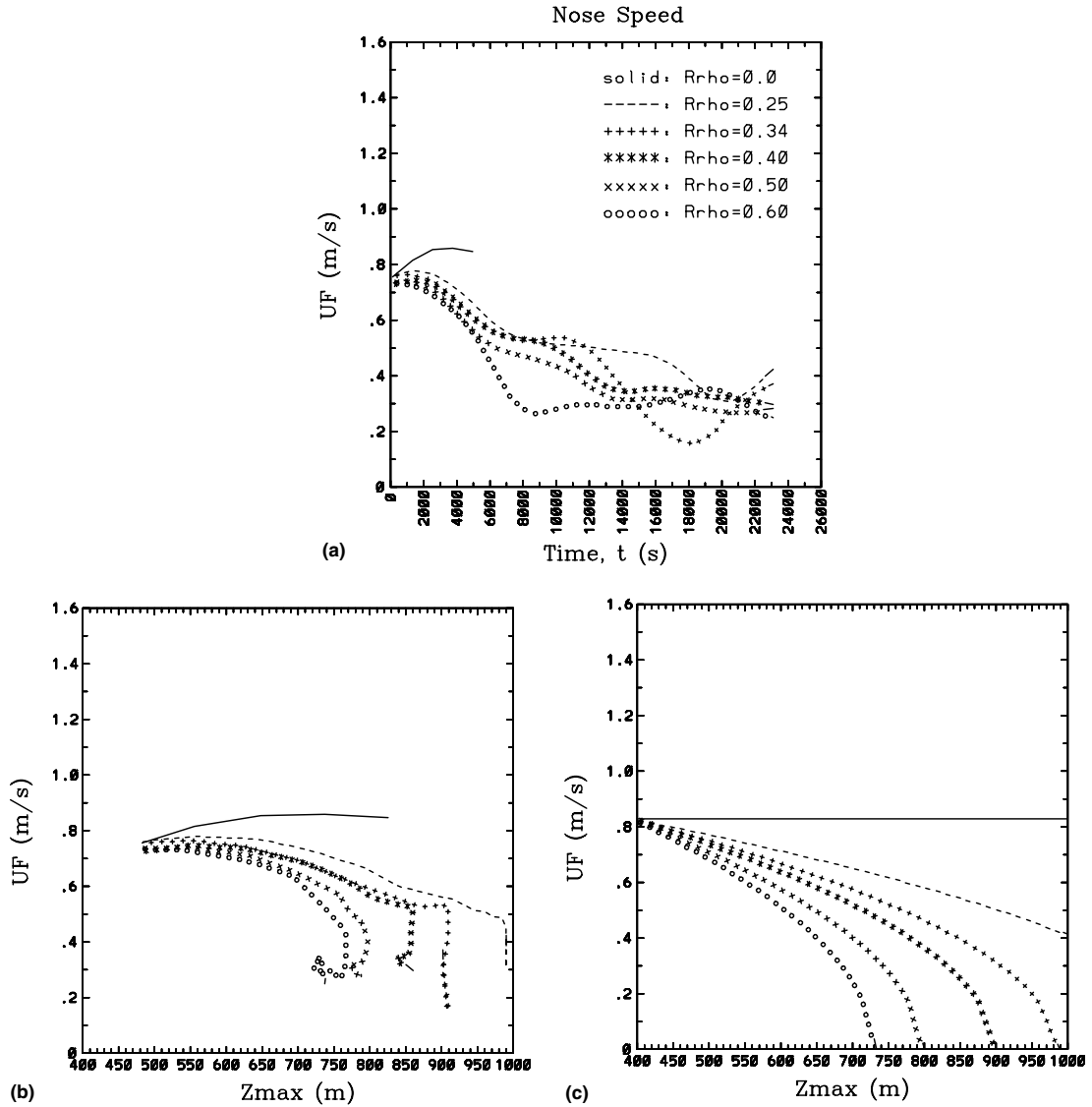


Fig. 7. (a) Propagation speed U_F as a function of time for experiments with $\theta = 5^\circ$; (b) U_F as a function of maximum depth z'_{max} in these experiments, and (c) U_F as a function of maximum distance z'_{max} as estimated from (12). Solid line shows the experiment with $R_\rho = 0$, dashed line the experiment with $R_\rho = 0.25$, line with “+++” the experiment with $R_\rho = 0.34$, line with “****” the experiment with $R_\rho = 0.40$, line with “xxxx” the experiment with $R_\rho = 0.50$, and line with “ooo” the experiment with $R_\rho = 0.60$, respectively.

$$\frac{U_F}{\sqrt{g\beta\Delta Sh_o}} = \frac{1}{\sqrt{2}} \sqrt{1 - R_\rho \frac{z' - h_i}{h_o}} \quad \text{for } h_i \leq z' \leq h_i + \frac{h_o}{R_\rho}. \quad (12)$$

$U_F(z')$ obtained from (12) is plotted in Fig. 7c, which shows the gradual deceleration of the gravity currents as they descend in an ambient fluid that gets denser with increasing depth. The

propagation stops when the density difference disappears at the separation depth of $z' = h_i + \frac{h_o}{R_\rho}$. Formula (12) does not account for continued propagation of gravity currents at the equilibrium depth, by mass conservation, and inertial effects, which bring the curves closer together in Fig. 7b, but otherwise it provides a simple explanation for the observed behavior of the propagation speed of the gravity currents.

5.4. Product salinity

The main emphasis of this study is to determine the properties of the equilibrated product water mass. Here we focus on the overflow salinity, which is the distinguishing property of the overflow in these experiments. The salinity of the product water mass, S_P , is calculated by averaging salinity over a tunnel of length ℓ after the separation point:

$$S_P(t) = \frac{1}{L_y} \frac{1}{x_2 - x_1} \int_0^{L_y} \int_{x_1}^{x_2} \frac{1}{h(x', y', t)} \int_{z_b(x')}^H S(x', y', z', t) \delta(x', y', z', t) dz' dx' dy', \quad (13)$$

where z_b is the bottom level, $x_1 = x_s$ is the actual separation point, and $x_2 = x_s + \ell$, with $\ell = 3$ km being the length of averaging after separation. H is the thickness of the overflow defined as

$$h(x, y, t) \equiv \int_{z_b}^H \delta(x, y, z', t) dz' \quad \text{where} \quad \delta(x, y, z, t) = \begin{cases} 0, & \text{when } S(x, y, z, t) < \epsilon \\ 1, & \text{when } S(x, y, z, t) \geq \epsilon, \end{cases} \quad (14)$$

with $\epsilon = 0.2$ (Özgökmen et al., 2004a).

Similarly, source salinity S_S is calculated from $x_1 = 0$ to $x_2 = 0.5$ km. The source water masses have roughly uniform properties for all experiments, $S_S \approx 0.73$ (psu) (not shown; note that the average salinity of the product water mass S_P , is somewhat smaller than the maximum range ΔS , since the initialization and forcing are via a cosine function, given in Özgökmen et al., 2004a, rather than a step function).

$S_P(t)$ for all separating experiments is shown in Fig. 8. As θ decreases, it takes longer for the formation of separated tongue consisting of product water mass. Since the separation distance is a function of R_ρ (9), the time difference for experiments with different R_ρ also decreases with increasing θ . In all experiments, S_P attain a quasi-equilibrium level: $S_P \approx 0.53$ (psu) for $R_\rho = 0.34$, $S_P \approx 0.56$ (psu) for $R_\rho = 0.40$, $S_P \approx 0.61$ (psu) for $R_\rho = 0.50$, and $S_P \approx 0.66$ (psu) for $R_\rho = 0.60$. Hence, as R_ρ increases, S_P increases, indicating that mixing is suppressed by the ambient stratification. Most interesting, $S_P \neq f(\theta)$, as pointed out also in Section 5.1 based on Fig. 5.

An explanation for the independence of S_P from the slope angle is as follows: Over a distance of x , the mass transport (per unit width) of the overflow $Q(x, t)$ becomes

$$Q(x, t) = Q(0, t) + w_E(\theta, R_\rho, t)x, \quad (15)$$

where $w_E(\theta, R_\rho, t)$ is the net entrainment velocity over the distance x . Generally speaking, one can anticipate the transport to vary significantly in time. To remove time-dependent fluctuations

$$\overline{\delta Q(x)} = \overline{Q(x, t) - Q(0, t)} = \overline{w_E(\theta, R_\rho)x}, \quad (16)$$

where the overline denotes time averaging.

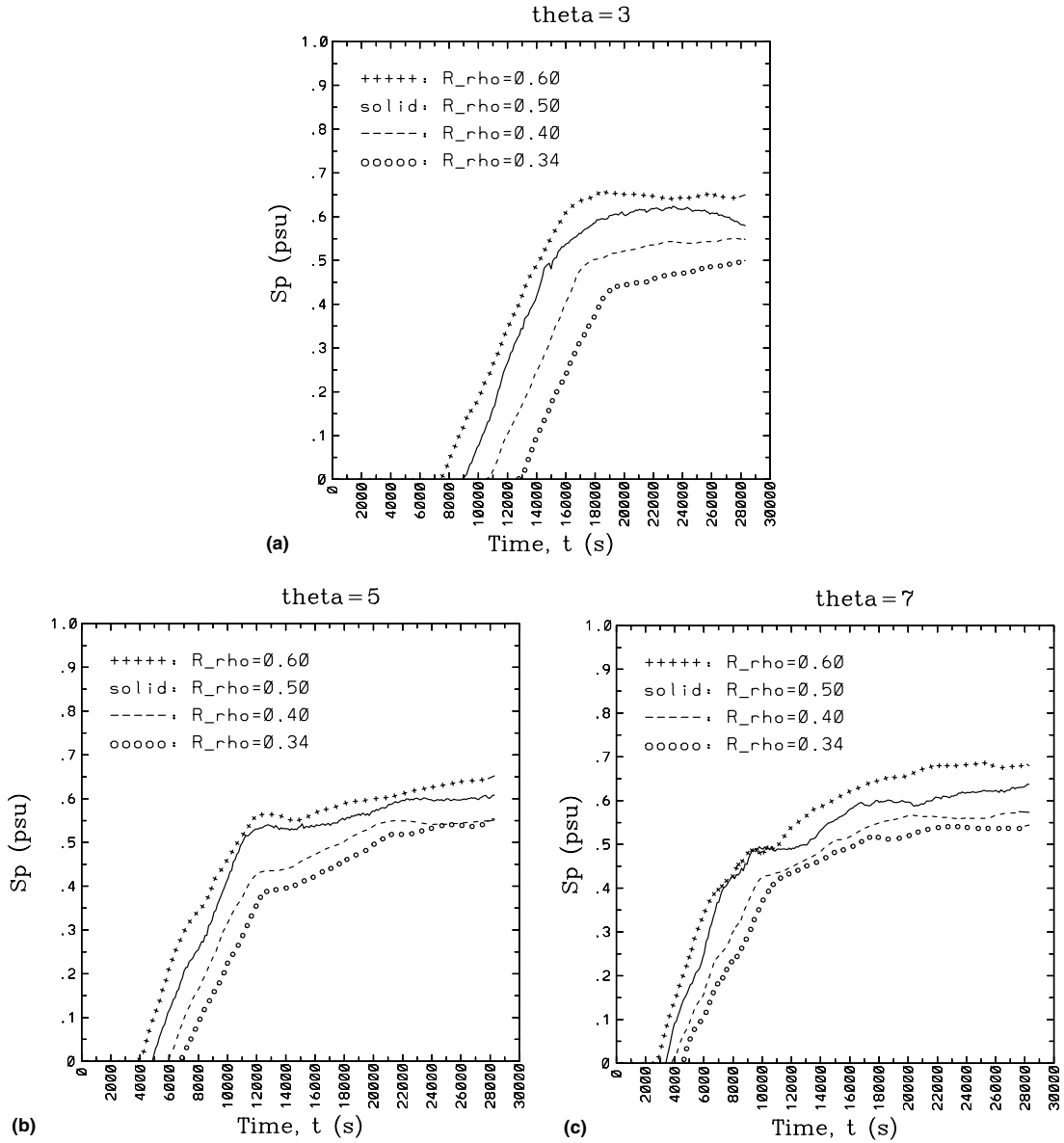


Fig. 8. Time evolution of product salinity $S_p(t)$ in experiments with slope angles of: (a) $\theta = 3^\circ$; (b) $\theta = 5^\circ$ and (c) $\theta = 7^\circ$. Lines with “oooo”, dashed lines, solid lines, and lines “++++” denote experiments with $R_\rho = 0.34, R_\rho = 0.40, R_\rho = 0.50$, and $R_\rho = 0.60$, respectively.

To explain the independence of product salinity from the slope angle, we assume that

$$\overline{w_E(\theta, R_\rho)} = w_1(\theta)w_2(R_\rho) \tag{17}$$

and, based on Turner (1986), Özgökmen and Chassignet (2002), Özgökmen et al. (2003) that

$$w_1(\theta) \approx a\theta, \tag{18}$$

where a is a constant. At the separation point (from (9)),

$$x_s \approx \frac{h_o}{R_\rho \tan \theta}, \quad (19)$$

the change in transport becomes

$$\overline{\delta Q(x_s)} \approx a\theta w_2(R_\rho) \frac{h_o}{R_\rho \tan \theta} \quad (20)$$

and since $\tan \theta \approx \theta$ for small θ ,

$$\overline{\delta Q(x_s)} \approx f(R_\rho) \neq f(\theta) \quad (21)$$

from which we conclude that $S_P \neq f(\theta)$. In other words, the current has to travel a shorter (longer) distance to separate when θ is increased (reduced), and the total entrained mass flux is exactly compensated.

Eq. (21) calls for several remarks. First, in order to obtain independence of the increase of transport from slope angle, the dependence of entrainment on slope angle needs to be captured. Second, (21) holds only in the case of simple topography, such that (18) is valid, and linear ambient stratification, such that (19) is valid. Complex bottom topography and ambient stratification should lead to θ -dependent $\overline{\delta Q(x_s)}$. Third, (21) is only a conjecture at this stage; its validity in these experiments is shown in the next section.

5.5. Transport and entrainment

The transports of the gravity currents $Q(x,t)$ are calculated and examples in a matrix of two slope angles of $\theta = 5^\circ$ and $\theta = 7^\circ$ and two density ratios of $R_\rho = 0.34$ and $R_\rho = 0.60$ are depicted in the form of Hovmoeller diagrams in Fig. 9. For instance, the case for $\theta = 5^\circ$ and $R_\rho = 0.34$ in Fig. 9a shows that near the inlet $x=0$ the transport remains approximately constant at $Q \approx 110 \text{ m}^2 \text{ s}^{-1}$ in time. The transport change along the current occurs first as a result of the passage of the characteristic head, which has the highest signal with the transport reaching $Q = 200 \text{ m}^2 \text{ s}^{-1}$, and then via regular high-frequency events associated with the Kelvin–Helmholtz rolls, the combination of which then leads to dramatic increases in transport downstream of their location. In general, there is a significant variability in time in the transport of the current. The change in the initial propagation speed upstream and downstream of the separation point x_s is also visible. When R_ρ is increased (Fig. 9b), the entrainment reduces. When θ is increased (Fig. 9c and d), no significant differences become apparent in the transport maps.

The following procedure is applied next: the transport increase of the overflow between the inlet location $x = 0$ and the separation point x_s , $\overline{\delta Q(x_s)}$ is calculated from (16) for all experiments. In experiments that do not lead to separation, namely, those with $R_\rho = 0$ and $R_\rho = 0.25$, the end of the slope, $x_s = x_{\text{slope}} = (H - h_i) / \tan \theta$ is taken as the segment over which the entrainment is averaged. $\overline{\delta Q(x_s)}$ normalized by the inlet average transport $\overline{Q(x=0)}$ is shown in Fig. 10a for all experiments as a function of θ and R_ρ . In homogeneous experiments with $R_\rho = 0$, $\overline{\delta Q(x_s)} / \overline{Q(x=0)}$ exceeds unity, that is, a doubling of transport by the time the gravity currents reach the end of the slope. As R_ρ increases, the entrainment decreases. Most important, there is no significant change in entrainment as a function of θ , and therefore the validity of (21) is confirmed.

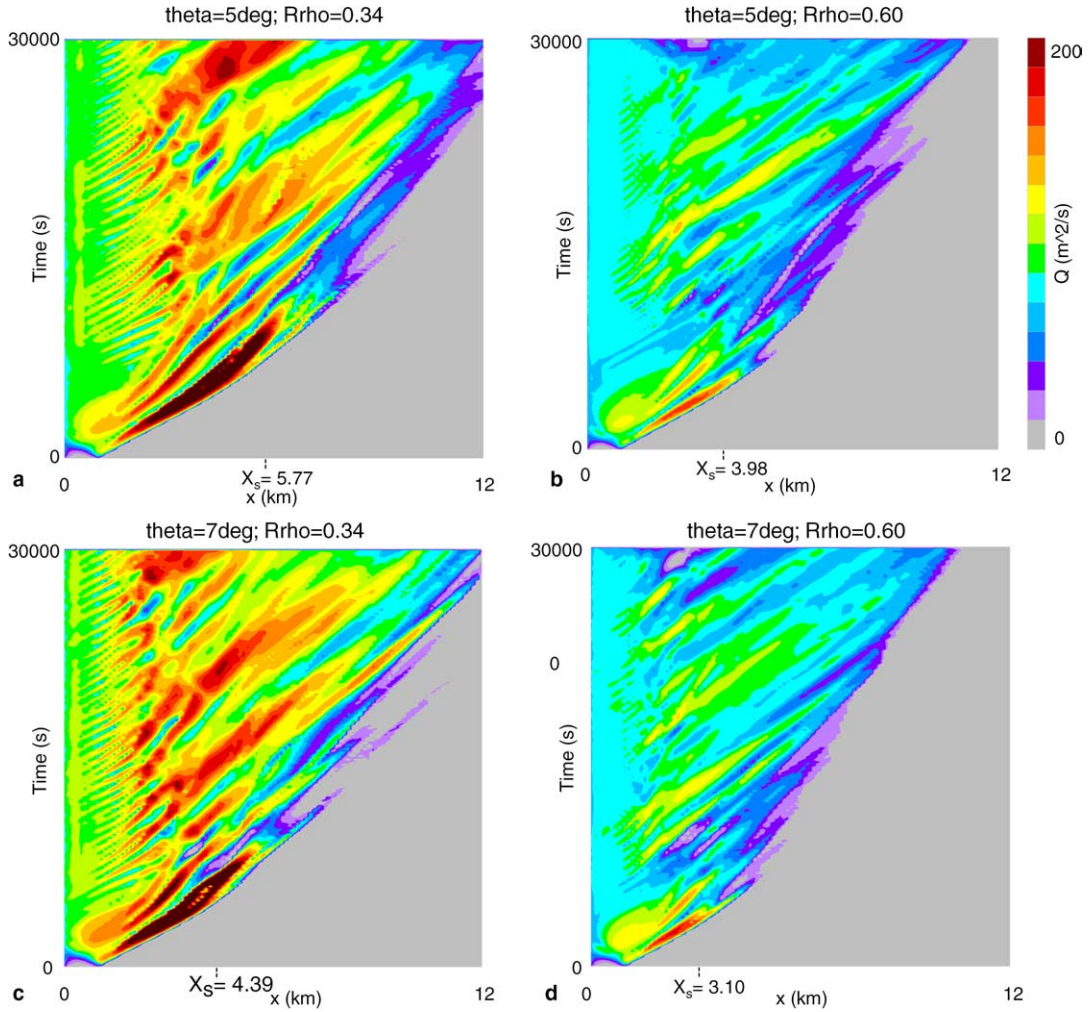


Fig. 9. Hovmoeller diagrams of the overflow mass transport $Q(x, t)$ (in $\text{m}^2 \text{s}^{-1}$) in selected experiments: (a) $\theta = 5^\circ$, $R_\rho = 0.34$; (b) $\theta = 5^\circ$, $R_\rho = 0.60$; (c) $\theta = 5^\circ$, $R_\rho = 0.34$ and (d) $\theta = 7^\circ$, $R_\rho = 0.60$. The separation distance x_s is marked for each case.

A simple regression to data in Fig. 10a yields

$$\frac{\overline{\delta Q(x_s)}}{\overline{Q(x=0)}} \approx 1.2 \exp(-R_\rho/0.25). \tag{22}$$

Next, the net average entrainment velocity over a distance of x_s is estimated from (via (16))

$$w_E(\theta, R_\rho) = \frac{\overline{\delta Q(x_s)}}{x_s} \tag{23}$$

and plotted in Fig. 10b, which justifies the separation of $\overline{w_E(\theta, R_\rho)}$ in the form of (17).

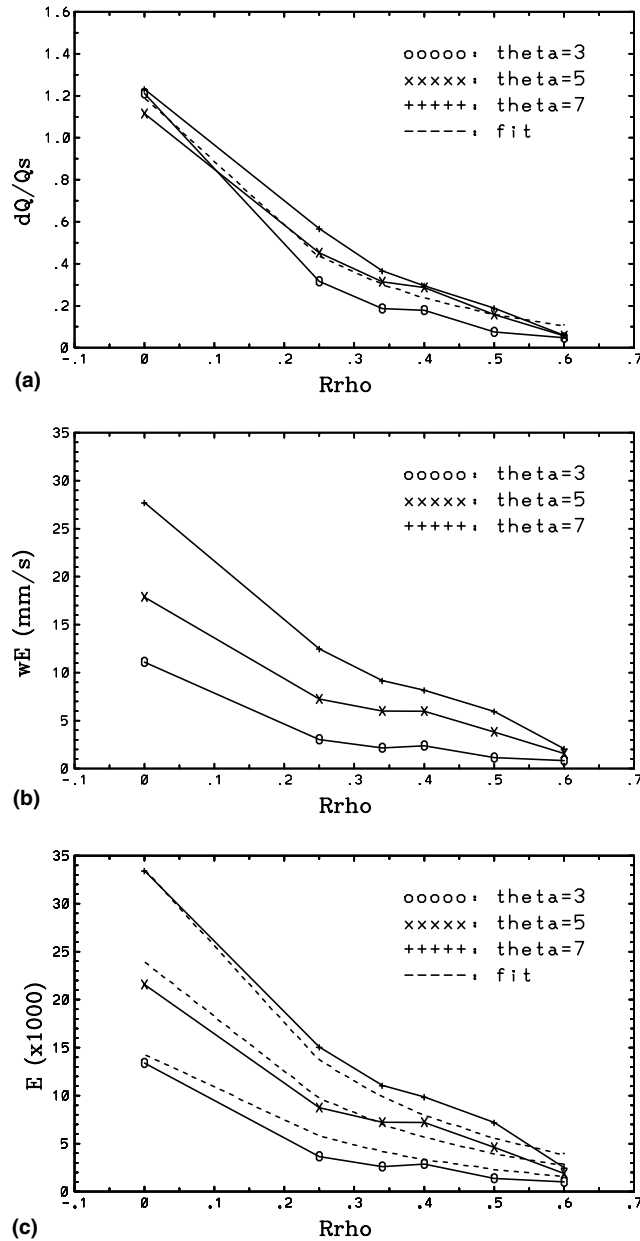


Fig. 10. (a) Normalized transport change $\overline{\delta Q(x_s)}/\overline{Q(x=0)}$; (b) net entrainment velocity $\overline{w_E}$ and (c) entrainment parameter E as a function of θ and $R\rho$ in all experiments. The dashed lines show the regression to data, $\overline{\delta Q(x_s)}/\overline{Q(x=0)} \approx 1.2 \exp(-R\rho/0.28)$ in (a), and $E \approx 4.83 \times 10^{-3} \theta \exp(-R\rho/0.25)$ in (c).

The net entrainment velocity is normalized by a known U , the speed of the gravity current based on upstream conditions, $U_o = \sqrt{g\beta\Delta Sh_o/2}$ (from Section 5.2). Following Morton et al. (1956) an entrainment parameter is defined as

$$E \equiv \frac{\overline{w_E}}{U_o}. \tag{24}$$

E is illustrated in Fig. 10c. A simple regression to data in the form of $E \approx b_1\theta \exp(-R_\rho/b_2)$ yields

$$E \approx 4.83 \times 10^{-3} \theta \exp(-R_\rho/0.28). \tag{25}$$

When $R_\rho = 0$, Eq. (25) reduces to $E \approx 4.83 \times 10^{-3}\theta$, in which case the classical θ -dependence of the entrainment parameter (e.g., Ellison and Turner, 1959; Turner, 1986; Price and Baringer, 1994) is recovered. This is also in reasonable quantitative agreement with $E \approx 3.5 \times 10^{-3}\theta$ obtained in Özgökmen et al. (2003) based on 2D modeling of the Red Sea overflow in an unstratified channel. It should be also mentioned that the entrainment parameter is traditionally characterized using the bulk Richardson number Ri (Ellison and Turner, 1959; Turner, 1986; Baines, 2001). While the dependence of mixing in stably-stratified flows to local shear Ri has a solid theoretical (Miles, 1961) and laboratory (Rohr et al., 1988; Fernando, 1991) support, the relationship between bulk and local shear Ri is not clear and the definition of bulk Ri has some ambiguity. It is assumed here that when the gravity current is mixing, the entrainment parameter is primarily a function of the slope angle (see also Fig. 7 in Ellison and Turner, 1959). Ri -dependent entrainment schemes can capture also regimes in which entrainment terminates, and they are more fundamental in some sense.

To bring everything together, we consider the mass and salt transport balances for separating bottom gravity currents in equilibrium (Fig. 11)

$$Q_S + Q_E = Q_P, \tag{26}$$

$$Q_S S_S + Q_E S_a = Q_P S_P, \tag{27}$$

where the source mass transport $Q_S \approx 110 \text{ m}^2 \text{ s}^{-1}$, source salinity $S_S \approx 0.73 \text{ psu}$, and ambient salinity $S_a = 0$ are assumed to be known, and the entrained mass transport Q_E , product mass transport Q_P and product salinity S_P are estimated from (26), (27), and the diagnostic fit from (22). The diagnostic fit is rewritten as

$$Q_E \approx Q_S f(R_\rho), \tag{28}$$

where

$$f(R_\rho) \approx 1.2 \exp(-R_\rho/0.25). \tag{29}$$

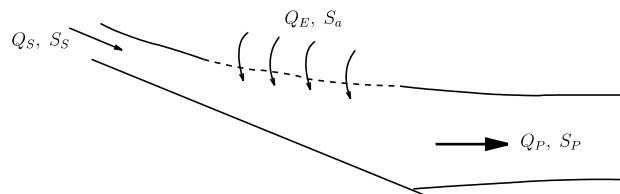


Fig. 11. Schematic depiction of the transformation of source water with a mass transport of Q_S and salinity S_S to equilibrated product water with mass transport Q_P and salinity S_P via the entrainment mass transport Q_E of the ambient salinity S_a .

From (26)

$$Q_P \approx Q_S[1 + f(R_\rho)] \quad (30)$$

and from (27),

$$S_P \approx S_S[1 + f(R_\rho)]^{-1}. \quad (31)$$

For comparison, data from Fig. 8 shows

$$S_P = \begin{cases} 0.53 \pm 0.02 & \text{when } R_\rho = 0.34, \\ 0.56 \pm 0.01 & \text{when } R_\rho = 0.40, \\ 0.61 \pm 0.02 & \text{when } R_\rho = 0.50, \\ 0.66 \pm 0.02 & \text{when } R_\rho = 0.60, \end{cases} \quad (32)$$

whereas (31) yields

$$S_P \approx \begin{cases} 0.55, & \text{when } R_\rho = 0.34, \\ 0.59, & \text{when } R_\rho = 0.40, \\ 0.63, & \text{when } R_\rho = 0.50, \\ 0.66, & \text{when } R_\rho = 0.60 \end{cases} \quad (33)$$

with the differences from (32) being due to regression errors in the fitting function (29). Hence, Eqs. (25) and (28)–(31) approximate the entrainment parameter, entrainment mass transport, product mass transport, and product salinity in these experiments.

5.6. 2D versus 3D

Since the above results are all based on 2D experiments, a 3D experiment is carried out in order to quantify the differences. The experiment is configured by extending the domain in the lateral direction and introducing a sinusoidal perturbation in the initial conditions (Fig. 1d), as outlined in Section 4 and with the parameters of $\theta = 7^\circ$ and $R_\rho = 0.5$. The time evolution of the 3D case is depicted in Fig. 4, whereas that from the equivalent 2D experiment is shown in Fig. 2.

Figs. 12a–c illustrate the time evolutions of the maximum levels of the salinity tongue $z_{\max}(t)$, the propagation distance of the salinity signal $X_F(t)$, and the product salinity $S_P(t)$ in both 2D and 3D versions of this experiment. Hovmoeller digrams of the gravity current mass transport $Q(x, t)$ are depicted in Fig. 13. Calculations are based on the spanwise-averaged velocity and salinity profiles from 3D output. The differences between the results from 2D and 3D versions for these diagnostics are small. The reason appears to be that the forcing, topography, and boundary conditions do not introduce any 3D motion, and the impact of the difference between 2D and 3D turbulence because of the differences in the initial conditions and equations of motions seems to be small. Therefore, we conclude that results based on 2D equations of motion are adequate for this experimental configuration.

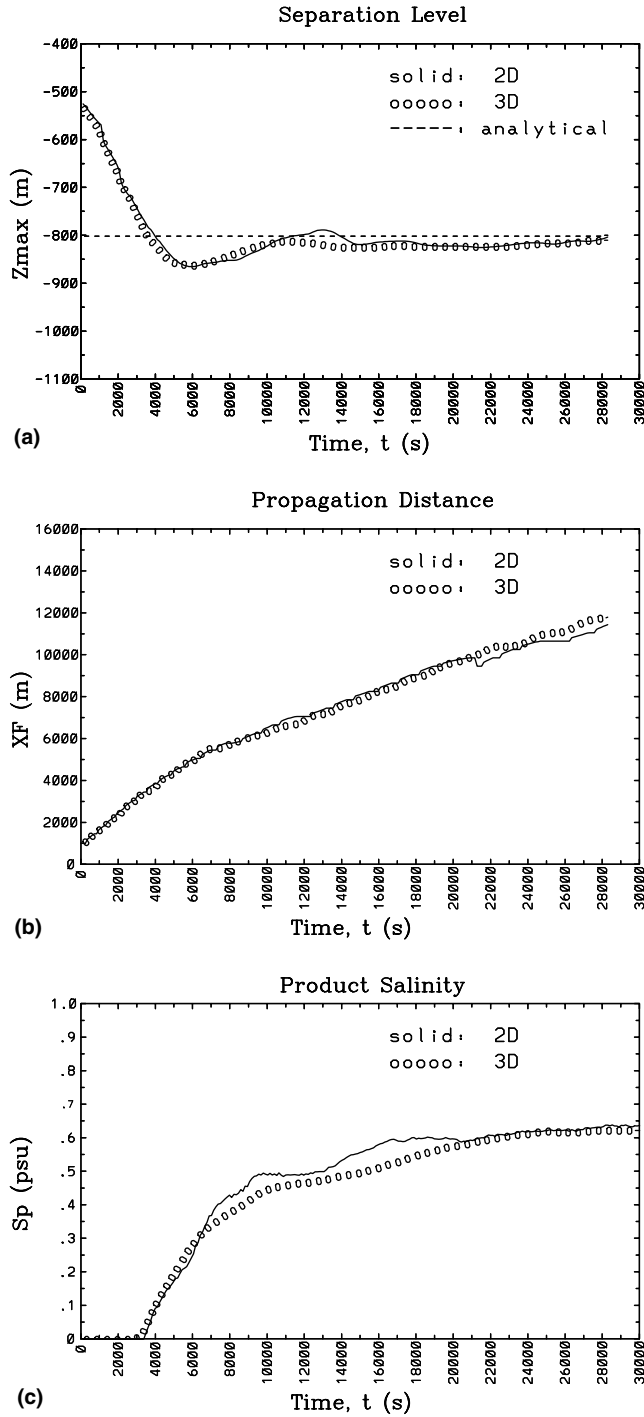


Fig. 12. (a) Maximum depths of the salinity signal as a function of time, (b) propagation position $X_F(t)$, and (c) product salinity $S_p(t)$ in 2D (solid lines) and 3D (lines with “ $\circ\circ\circ$ ”) experiments of the case with $\theta = 7^\circ$, $R_p = 0.50$.

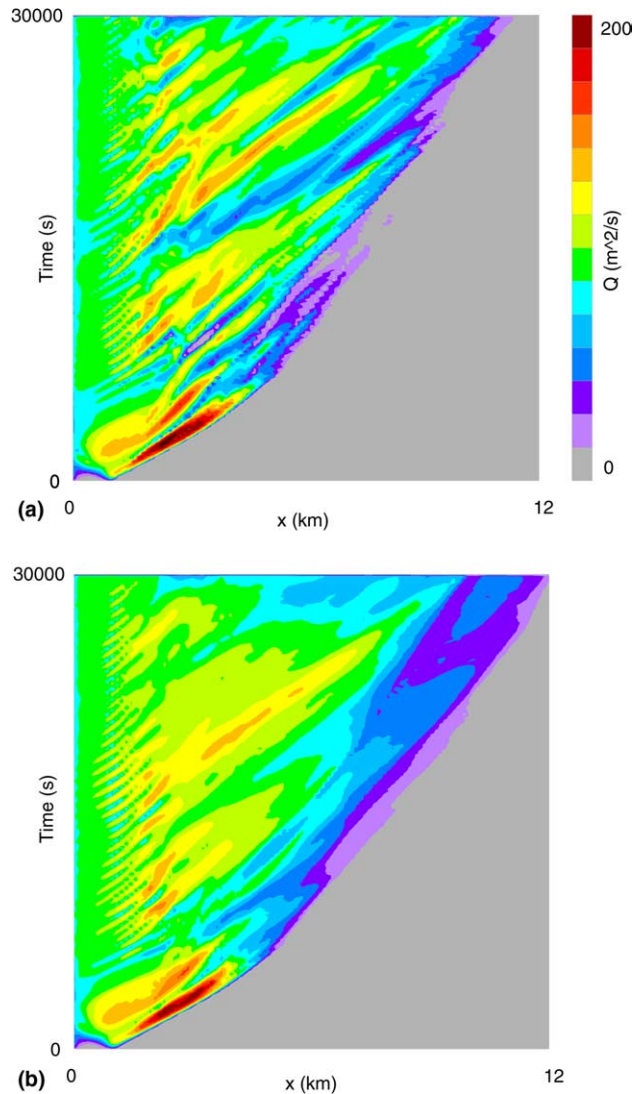


Fig. 13. Hovmoeller diagrams of the overflow mass transport $Q(x,t)$ (in m^2s^{-1}) in (a) 2D, and (b) 3D experiments of the case with $\theta = 7^\circ$, $R_\rho = 0.50$.

6. Summary and conclusions

Our understanding of the dynamics of overflows is based on the results of dedicated observational programs in the Mediterranean Sea overflow (Baringer and Price, 1997a,b), Denmark Strait overflow (Girton et al., 2003; Girton and Sanford, 2003), Red Sea overflow (Peters et al., 2005; Peters and Johns, 2005), Faroe Bank Channel (Price, 2004), and Antarctic Ocean (Gordon et al., 2004) and also of laboratory tank experiments (e.g., Ellison and Turner, 1959; Simpson, 1987; Hallworth et al., 1996; Monaghan et al., 1999; Baines, 2001, 2005; Cenedese et al., 2004)

and process modeling studies (e.g., Özgökmen and Chassignet, 2002; Özgökmen et al., 2003; Özgökmen et al., 2004a,b; Chang et al., in press). It is important that this knowledge be incorporated in OGCMs in the form of appropriate mixing parameterizations because of the pressing need to better represent gravity current entrainment in OGCMs and climate-related modeling studies.

In this study, the behavior of turbulent gravity currents in the presence of ambient stratification is studied by numerical simulation, for cases in which equilibrated product water masses are formed. The main objective is to explore how the ambient stratification affects entrainment and the properties of product water masses, which are of ultimate interest for ocean and climate modelers.

Numerical experiments are conducted with the high-order nonhydrostatic spectral element model Nek5000. The model is configured by placing a high-salinity water mass on top of a constant-slope topography. The interior is initialized by using a linear temperature distribution. A total of 18 experiments are conducted, consisting of three different slope angles and six different ambient stratification parameters. Twelve experiments are configured such that gravity currents detach from the bottom and form the so-called product water masses, with nearly equilibrated properties. The remaining experiments include cases with weak stratification that do not exhibit separation from the bottom within the limits of the domain and cases with a homogeneous ambient as reference experiments. Investigations include how the strength of the ambient stratification and the slope angle affect the separation level of the current from the bottom, the propagation speed, the salinity of the product water masses, and the transport and entrainment of the gravity current.

The propagation speed is calculated and found to decrease as gravity currents descend into denser ambient fluid and lose their density contrast. The propagation speed is well approximated by a simple relationship (12) until the separation level.

The averaged salinity of the product water masses is calculated and observed to be approximately independent of the slope angle. The reason is a simple geometric artifact: the current has to travel a shorter (longer) distance to reach the level of neutral buoyancy when θ is increased (reduced), and the total entrained mass flux is exactly compensated. The reason is that, in the case of constant-slope topography, the entrainment velocity is linearly proportional to θ , and in the case of linear ambient stratification, the distance to separation is inversely proportional to θ (for small θ). Because of this simplification, the entrainment mass transport Q_E , product mass transport Q_P , and product salinity S_P depend only on the ambient stratification parameter R_ρ , and these quantities are approximated as simple algebraic functions of R_ρ in Eqs. (28)–(31) that modify the source properties Q_S and S_S . The entrainment parameter E is expressed as a function of θ and R_ρ in Eq. (25).

Since these results are based on 2D simulations, a 3D simulation is conducted and shown not to differ significantly from the 2D case regarding these integrated quantities, as the forcing, boundary conditions and bottom topography do not induce 3D motion.

Moreover, it is found that the separation level is well estimated by calculating where the densest overflow water would equilibrate in the ambient fluid in the absence of mixing. The reason is that in most cases the mixing layer does not penetrate all the way to the bottom of the gravity current, and the densest bottom salinity remains nearly undiluted until the separation level is reached. For high R_ρ , the so-called overshoot and springback phenomenon is observed, whereas as R_ρ gets smaller, mixing affects the entire gravity current and causes early separation. It is well known, for instance, that the Mediterranean overflow is dense enough to sink the bottom of the North

Atlantic Ocean, and it undergoes significant dilution to settle at mid-depths (e.g., Baringer and Price, 1997a).

We plan to address several issues in the immediate future to bridge the gap between our process studies and oceanic observations. The first is related to the parameter range of R_ρ . The present domain configuration restricts the weakest stratification with gravity current separation to be $R_\rho = 1/3$. In order to investigate the regime with more vigorous mixing, which can significantly impact the separation level, the domain depth needs to be increased such that separation and product water mass formation with smaller R_ρ can be captured. This is essential to investigate the parameter regime in which mixing from the top to the bottom of the plume is enhanced. Alternatively, mixing near the bottom can be responsible for dilution of the densest part of the plume. We plan to pursue this hypothesis by introducing bumps on the topography, as a follow-up study of Özgökmen et al. (2004b), but with emphasis on product water mass formation. In addition, we will study the impact of complex ambient stratification.

Acknowledgement

We greatly appreciate the support of National Science Foundation via grants OCE 0336799 and DMS 0209326, the Office of Naval Research grant N00014-03-1-0425 and the Mathematical, Information, and Computational Sciences Division subprogram of the Office of Advanced Scientific Computing Research, U.S. Department of Energy, under Contract W-31-109-ENG-38. We benefited greatly from discussions with the other PIs of the Climate Process Team on gravity current entrainment, E. Chassignet, G. Danabasoglu, T. Ezer, A. Gordon, S. Griffies, R. Hallberg, W. Large, S. Legg, H. Peters, J. Price, P. Schopf and J. Yang, as well as with P. Baines and M. Wells. We thank Gail Pieper for the careful technical editing of the manuscript. We also thank two anonymous reviewers for their constructive comments, which helped improve the manuscript.

References

- Baines, P.G., 2001. Mixing in flows down gentle slopes into stratified environments. *J. Fluid Mech.* 443, 237–270.
- Baines, P.G., 2002. Two-dimensional plumes in stratified environments. *J. Fluid Mech.* 471, 315–337.
- Baines, P.G., 2005. Mixing regimes for the flow of dense fluid down slopes into stratified environments. *J. Fluid Mech.* 538, 245–267.
- Baringer, M.O., Price, J.F., 1997a. Mixing and spreading of the Mediterranean out-flow. *J. Phys. Oceanogr.* 27, 1654–1677.
- Baringer, M.O., Price, J.F., 1997b. Momentum and energy balance of the Mediterranean outflow. *J. Phys. Oceanogr.* 27, 1678–1692.
- Beckmann, A., Döscher, R., 1997. A method for improved representation of dense water spreading over topography in geopotential-coordinate models. *J. Phys. Oceanogr.* 27, 581–591.
- Benjamin, T.B., 1968. Gravity currents and related phenomena. *J. Fluid Mech.* 31, 209–248.
- Bloomfield, L.J., Kerr, R., 1998. Turbulent fountains in a stratified fluid. *J. Fluid Mech.* 358, 335–356.
- Bower, A.S., Hunt, H.D., Price, J.F., 2000. Character and dynamics of the Red Sea and Persian Gulf outflows. *J. Geophys. Res.* 105, 6387–6414.

- Bower, A., Serra, N., Ambar, I., 2002. Structure of the Mediterranean undercurrent and Mediterranean water spreading around the southwestern Iberian peninsula. *J. Geophys. Res. Oceans* 107 (C10) (no. 3160).
- Britter, R.E., Linden, P.F., 1980. The motion of the front of a gravity current traveling down an incline. *J. Fluid Mech.* 99, 531–543.
- Cenedese, C., Whitehead, J.A., Ascarelli, T.A., Ohiwa, M., 2004. A dense current flowing down a sloping bottom in a rotating fluid. *J. Phys. Oceanogr.* 34, 188–203.
- Chang, Y., Xu, X., Özgökmen, T.M., Chassignet, E.P., Peters, H., Fischer, P.F., in press. Comparison of gravity current mixing parameterizations and calibration using a high-resolution 3D nonhydrostatic spectral element model. *Ocean Model.*
- Corcos, G.M., Sherman, F.S., 1984. The mixing layer: deterministic models of a turbulent flow. Part I. Introduction and the two-dimensional flow. *J. Fluid Mech.* 139, 29–65.
- Dryja, M., Widlund, O.B., 1987. An additive variant of the Schwarz alternating method for the case of many subregions. Technical Report 339, Department of Computer Science, Courant Institute.
- Ellison, T.H., Turner, J.S., 1959. Turbulent entrainment in stratified flows. *J. Fluid Mech.* 6, 423–448.
- Ezer, T., 2005. Entrainment, diapycnal mixing and transport in three-dimensional bottom gravity current simulations using the Mellor–Yamada turbulence scheme. *Ocean Model* 9, 151–168.
- Ezer, T., Mellor, G.L., 2004. A generalized coordinate ocean model and comparison of the bottom boundary layer dynamics in terrain-following and in z-level grids. *Ocean Model.* 6, 379–403.
- Fernando, H.J.S., 1991. Turbulent mixing in stratified fluids. *Annu. Rev. Fluid Mech.* 23, 455–493.
- Fischer, P.F., 1997. An overlapping Schwarz method for spectral element solution of the incompressible Navier–Stokes equations. *J. Comput. Phys.* 133, 84–101.
- Fischer, P.F., Mullen, J.S., 2001. Filter-based stabilization of spectral element methods. *C.R. Acad. Sci. Paris Ser. I—Anal. Numer.* 332, 265–270.
- Fischer, P.F., Miller, N.I., Tufo, H.M., 2000. An overlapping Schwarz method for spectral element simulation of three-dimensional incompressible flows. In: Björstad, P., Luskin, M. (Eds.), *Parallel Solution of Partial Differential Equations*. Springer-Verlag, Berlin, pp. 159–181.
- Flierl, G.R., Stern, M.E., Whitehead, J.A., 1981. The physical significance of modons: laboratory experiments and general integral constraints. *Dyn. Atmos. Oceans* 7, 233–263.
- Gargett, A.E., 1984. Vertical diffusivity in the ocean interior. *J. Mar. Res.* 42, 359–393.
- Girton, J.B., Sanford, T.B., 2003. Descent and modification of the overflow plume in the Denmark Strait. *J. Phys. Oceanogr.* 33, 1351–1363.
- Girton, J.B., Sanford, T.B., Käse, R.H., 2003. Synoptic sections of the Denmark Strait overflow. *Geophys. Res. Lett.* 28, 1619–1622.
- Gordon, A., Zambianchi, E., Orsi, A., Visbeck, M., Giulivi, C., Whitworth III, T., Spezie, G., 2004. Energetic plumes over the western Ross Sea continental slope. *Geophys. Res. Lett.* 31 (21) (no. L21302).
- Griffiths, R.W., 1986. Gravity currents in rotating systems. *Annu. Rev. Fluid Mech.* 18, 59–89.
- Hallberg, R., 2000. Time integration of diapycnal diffusion and Richardson number dependent mixing in isopycnal coordinate ocean models. *Mon. Wea. Rev.* 128 (5), 1402–1419.
- Hallworth, M.A., Huppert, H.E., Phillips, J.C., Spark, S.J., 1996. Entrainment into two-dimensional and axisymmetric turbulent gravity current. *J. Fluid Mech.* 308, 289–311.
- Johnson, G.C., Sanford, T.B., O’Neil Baringer, M., 1994a. Stress on the Mediterranean outflow plume: part I. Velocity and water property measurements. *J. Phys. Oceanogr.* 24, 2072–2083.
- Johnson, G.C., Lueck, R.G., Sanford, T.B., 1994b. Stress on the Mediterranean outflow plume: part II. Turbulent dissipation and shear measurements. *J. Phys. Oceanogr.* 24, 2084–2092.
- Jungclaus, J.H., Mellor, G., 2000. A three-dimensional model study of the Mediterranean outflow. *J. Mar. Sys.* 24, 41–66.
- Keulegan, G.H., 1958. The motion of saline fronts in still water. US Nat. Bur. Stand., Report no. 5831.
- Killworth, P.D., Edwards, N.R., 1999. A turbulent bottom boundary layer code for use in numerical ocean models. *J. Phys. Oceanogr.* 29, 1221–1238.
- Killworth, P.D., 1977. Mixing on the Weddell Sea continental slope. *Deep-Sea Res.* 24, 427–448.
- Large, W.G., McWilliams, J.C., Doney, S.C., 1994. Oceanic vertical mixing: a review and a model with a nonlocal boundary layer parameterization. *Rev. Geophys.* 32, 363–403.

- Legg, S., Hallberg, R.W., Girton, J.B., 2006. Comparison of entrainment in overflows simulated by z -coordinate, isopycnal and non-hydrostatic models. *Ocean Model.* 11, 69–97.
- Maday, Y., Patera, A.T., 1989. Spectral element methods for the Navier–Stokes equations. In: Noor, A.K. (Ed.), *State of the Art Surveys in Computational Mechanics*. ASME, New York, pp. 71–143.
- Maday, Y., Patera, A.T., Rønquist, E.M., 1990. An operator-integration-factor splitting method for time-dependent problems: application to incompressible fluid flow. *J. Sci. Comput.* 5 (4), 310–337.
- Marmorino, G.O., 1987. Observations of small-scale mixing processes in the seasonal thermocline, Part 2: Wave breaking. *J. Phys. Oceanogr.* 17, 1348–1355.
- Miles, J.W., 1961. On the stability of heterogeneous shear flows. *J. Fluid Mech.* 10, 496–508.
- Monaghan, J.J., Cas, R.A.F., Kos, A.M., Hallworth, M., 1999. Gravity currents descending a ramp in a stratified tank. *J. Fluid Mech.* 379, 39–70.
- Morton, B.R., Taylor, G.I., Turner, J.S., 1956. Turbulent gravitational convection from maintained and instantaneous sources. *Proc. R. Soc. Lond.* A234, 1–23.
- Nakano, H., Suginoara, N., 2002. Effects of bottom boundary layer parameterization on reproducing deep and bottom waters in a world ocean model. *J. Phys. Oceanogr.* 32, 1209–1227.
- Nielsen, A.H., Rasmussen, J.J., 1996. Formation and temporal evolution of the Lambdipole. *Phys. Fluids* 9, 982–991.
- Özgökmen, T.M., Chassignet, E., 2002. Dynamics of two-dimensional turbulent bottom gravity currents. *J. Phys. Oceanogr.* 32, 1460–1478.
- Özgökmen, T.M., Johns, W., Peters, H., Matt, S., 2003. Turbulent mixing in the Red Sea outflow plume from a high-resolution nonhydrostatic model. *J. Phys. Oceanogr.* 33 (8), 1846–1869.
- Özgökmen, T.M., Fischer, P.F., Duan, J., Iliescu, T., 2004a. Three-dimensional turbulent bottom density currents from a high-order nonhydrostatic spectral element model. *J. Phys. Oceanogr.* 34 (9), 2006–2026.
- Özgökmen, T.M., Fischer, P.F., Duan, J., Iliescu, T., 2004b. Entrainment in bottom gravity currents over complex topography from three-dimensional nonhydrostatic simulations. *Geophys. Res. Lett.* 31, L13212. doi:10.1029/2004GL020186.
- Papadakis, M.P., Chassignet, E.P., Hallberg, R.W., 2003. Numerical simulations of the Mediterranean Sea outflow: impact of the entrainment parameterization in an isopycnal coordinate ocean model. *Ocean Model.* 5, 325–356.
- Patera, A.T., 1984. A spectral element method for fluid dynamics; Laminar flow in a channel expansion. *J. Comput. Phys.* 54, 468–488.
- Peters, H., Johns, W.E., 2005. Mixing and entrainment in the Red Sea outflow plume. II. Turbulence characteristics. *J. Phys. Oceanogr.* 35, 584–600.
- Peters, H., Johns, W.E., Bower, A.S., Fratantoni, D.M., 2005. Mixing and entrainment in the Red Sea outflow plume. I. Plume structure. *J. Phys. Oceanogr.* 35, 569–583.
- Price, J.F., 2004. A process study of the Faroe Bank Channel overflow. *Geophys. Res. Abstracts* 6, 07788.
- Price, J.F., Baringer, M.O., 1994. Outflows and deep water production by marginal seas. *Prog. Oceanogr.* 33, 161–200.
- Price, J., Yang, J., 1998. Marginal sea overflows for climate simulations. In: Chassignet, E.P., Verron, J. (Eds.), *Ocean Modelling and Parameterization*, pp. 155–170.
- Price, J.F., Baringer, M.O., Lueck, R.G., Johnson, G.C., Ambar, I., Parrilla, G., Cantos, A., Kennelly, M.A., Sanford, T.B., 1993. Mediterranean outflow mixing and dynamics. *Science* 259, 1277–1282.
- Rohr, J.J., Itsweire, E.C., Helland, K.N., Van Atta, C.W., 1988. Growth and decay of turbulence in stably stratified shear flow. *J. Fluid Mech.* 195, 77–111.
- Schumann, U., Gerz, T., 1995. Turbulent mixing in stably stratified shear flows. *J. Appl. Met.* 34, 33–48.
- Simpson, J.E., 1987. *Gravity Currents in the Environment and the Laboratory*. John Wiley and Sons, New York, 244p.
- Simpson, J.E., 1982. Gravity currents in the laboratory, atmosphere, and the ocean. *Annu. Rev. Fluid Mech.* 14, 213–234.
- Simpson, J.E., 1969. A comparison between laboratory and atmospheric density currents. *Quart. J. Roy. Met. Soc.* 95, 758–765.
- Smagorinsky, J., 1963. General circulation experiments with the primitive equations, I. The basic experiment. *Mont. Weather Rev.* 91, 99–164.
- Smith, P.C., 1975. A streamtube model for bottom boundary currents in the ocean. *Deep-Sea Res.* 22, 853–873.

- Smith, R.A., 1991. Maximization of vortex entropy as an organizing principle in intermittent, decaying, two-dimensional turbulence. *Phys. Rev. A* 43, 1126–1129.
- Tufo, H.M., Fischer, P.F., 1999. Terascale spectral element algorithms and implementations. In: *Proceedings of the ACM/IEEE SC99 Conference on High Performance Networking and Computing*. IEEE Computer Society, Silver Spring, MD (Gordon Bell Prize submission).
- Tufo, H.M., Fischer, P.F., 2001. Fast parallel direct solvers for coarse grid problems. *J. Parallel Distr. Comput.* 61, 151–177.
- Turner, J.S., 1986. Turbulent entrainment: the development of the entrainment assumption, and its applications to geophysical flows. *J. Fluid Mech.* 173, 431–471.
- Webster, C.A.G., 1964. An experimental study of turbulence in a density stratified shear flow. *J. Fluid Mech.* 19, 221–245.
- Willebrand, J., Barnier, B., Böning, C., Dieterich, C., Harrmann, P., Killworth, P.D., LeProvost, C., Jia, Y., Molines, J.-M., New, A.L., 2001. Circulation characteristics in three eddy-permitting models of the North Atlantic. *Prog. Oceanogr.* 48, 123–161.
- Winton, M., Hallberg, R., Gnanadesikan, A., 1998. Simulation of density-driven frictional downslope flow in *z*-coordinate ocean models. *J. Phys. Oceanogr.* 28, 2163–2174.